

T.C. DOGUS UNIVERSITY

Institute of Science

**ELECTROMAGNETIC SCATTERED FIELD ANALYSIS OF 2D
WEDGE GEOMETRIES WITH HFA TECHNIQUES AND FDTD
METHOD**

M.Sc. Thesis

Mehmet Alper USLU

201092004

Thesis Supervisor: Prof.Dr. Levent SEVGI

Istanbul, January 2012

この を しんぴさんに ささげます...

ACKNOWLEDGEMENTS

I would like to express my deepest gratitude to my M.Sc. supervisor, Prof. Dr. Levent SEVGI, for his guidance and valuable help throughout the thesis. He provided me with a better understanding of many concepts as well as academic insight. His contributions will effect in the rest of my academic life. He is intelligent supervisor and an excellent person for all aspects.

I would like to thank Prof. Dr. Cem GOKNAR, Prof. Dr. Ergul AKCAKAYA, Prof. Dr. Ercan TOPUZ and Assist. Prof. Dr. Zekeriya UYKAN for their scientific contributions to my academic career.

I would like to also thank Assist. Prof. Dr. Cagatay ULUISIK for countless reasons. Most importantly, he was like a brother to me throughout all my graduate and undergraduate studies in Dogus University in the past 5.5 years. Without his guidance and support I cannot continue my academic career.

I would like to thank my friends and colleagues in Dogus University. My thanks go to Cihan AYDIN, Ozlem UNAN, Onur GUVENC, Bayram CEYHAN and Ahmet SEFER.

Finally, my special thanks go to my family for supporting me in every way they can.

ABSTRACT

In this thesis, electromagnetic scattered field analysis of two dimensional non-penetrable wedge geometry have been investigated with both high frequency asymptotic techniques (HFA) and finite difference time domain (FDTD) method.

Among HFA techniques, Physical optics (PO), Physical theory of diffraction (PTD), Unified theory of diffraction (UTD), Parabolic equation (PE), Exact series and Exact integral methods are applied to inspect electromagnetic scattering behavior of two dimensional non-penetrable wedge geometry analytically.

As a numerical technique, finite difference time domain (FDTD) method and the important aspects in its implementation are explained briefly. Also, absorbing boundary conditions and modeling issues are investigated. Meshing algorithm is developed to reduce staircase modeling errors which is formed by the application of standard Yee algorithm. In order to show the qualification of FDTD method, some examples are presented with HFA results.

A novel Matlab based softwares WEDGE GUI and WEDGE FDTD GUI are also presented with thesis. The former was developed to analyze two dimensional perfect electric conductor (PEC) wedge geometries with various HFA methods. The latter was developed to analyze same geometry with finite difference time domain (FDTD) method. Source codes of these programs can be found in the CD given with this thesis.

ÖZET

Bu tezde, kusursuz iletken yapıdaki üçgensel objelerden oluşan elektromanyetik saçılım alanları, yüksek frekans asimtotik teknikleri ve zaman domeninde sonlu farklar yöntemi ile incelenmiştir.

Yüksek frekans asimtotik tekniklerden, fiziksel optik, fiziksel difraksiyon teorisi, birleştirilmiş difraksiyon teorisi, parabolik denklem, seri ve integral metotları bu tip problemleri analitik olarak analiz etmek için uygulanmıştır.

Bir numerik teknik olan zaman domeninde sonlu farklar metodu ve bu metodun uygulanması da bu tez içerisinde detaylı bir şekilde anlatılmıştır. Yutucu sınır koşulları ve modelleme sorunları da ayrıca incelenmiştir. Standart Yee algoritmasının uygulanmasından dolayı oluşan modelleme hatalarını düşürmek için, hücreleme algoritması geliştirilmiştir. Zaman domeninde sonlu farklar yönteminin sonuçlarının doğruluğunu göstermek için birkaç örnek yüksek frekans asimtotik yöntemlerinin sonuçları ile birlikte verilmiştir.

Bu tez kapsamında, WEDGE GUI ve WEDGE FDTD GUI adında iki yeni matlab tabanlı program sunulmuştur. WEDGE GUI, 2 boyutlu kusursuz iletken üçgensel objeleri çeşitli yüksek frekans asimtotik teknikler ile kolay bir şekilde analiz etmek için geliştirilmiştir. WEDGE FDTD GUI ise aynı geometriyi zaman domeninde sonlu farklar yöntemi ile analiz etmek için tasarlanmıştır. Bu programların kaynak kodları tez ile birlikte verilen CD içerisinde bulunabilir.

Table of Contents

ACKNOWLEDGEMENTS	i
ABSTRACT	ii
ÖZET	iii
ABBREVIATIONS	v
LIST OF FIGURES	vii
1 INTRODUCTION	1
1.1 Outline of the Thesis	2
2 ANALYTICAL METHODS	3
2.1 Introduction	3
2.2 Plane Wave Illumination and HFA Models.....	5
2.3 HFA Models under Line Source Excitations.....	11
2.4 The WedgeGUI Virtual Tool and Some Examples	13
2.5 Conclusions	18
3 FINITE DIFFERENCE TIME DOMAIN (FDTD) METHOD	19
3.1 Introduction	19
3.2 3D FDTD Algorithm.....	21
3.3 Reduction to 2D TE and TM Modes	27
3.4 Numerical Dispersion	30
3.5 Stability.....	34
3.6 Perfectly Matched Layer Boundary Conditions	35
3.7 Modeling PEC Objects	53
3.8 Calculation of Diffracted Fields for Wedge Type Object.....	57
3.9 WEDGE FDTD GUI and Simulation Examples	58
3.10 Conclusions	60
4 CONCLUSIONS AND FUTURE RESEARCH	62
4.1 Summary	62
4.2 Future Work	63
REFERENCES	64
APPENDIX I	67
BIOGRAPHY	72

ABBREVIATIONS

$2D$	Two Dimensional
$3D$	Three Dimensional
\mathbf{B}	Magnetic flux density vector
\mathbf{D}	Electric flux density vector
f	Frequency
\mathbf{H}	Magnetic field intensity vector
j	Imaginary unit
$j^{(0)}$	Uniform surface currents generated by the incident field
$j^{(1)}$	Non-uniform surface currents generated by the incident field
\mathbf{J}	Electric current density vector
\mathbf{k}	Wave vector
\mathbf{M}	Magnetic current density vector
$u_s^{exact} \equiv E_z^{exact}$	Exact solution for the soft (TM) boundary conditions
$u_h^{exact} \equiv H_z^{exact}$	Exact solution for the hard (TE) boundary conditions
u_0	Amplitude of incident field
u^{GO}	Geometrical optics total fields (sum of the incident and reflected fields)
u_d^{exact}	Diffracted fields (i.e., exact total field solution minus the Geometrical Optics fields)
u^{PO}	Physical Optics total fields
u^{PTD}	Physical Theory of Diffraction total fields
$u^{d,PO}$	Physical Optics diffracted fields (i.e. Physical optics total fields minus the Geometric Optics fields)
$u^{d,PTD}$	Physical Theory of Diffraction diffracted fields (i.e. Physical Theory of Diffraction total fields minus the Geometric Optics fields)
∇	Gradient
$\nabla \times$	Curl
ϵ	Electrical permittivity
ϵ_r	Relative electrical permittivity
μ	Magnetic permeability
σ	Electrical conductivity
ω	Wave angular frequency

ABC	Absorbing boundary condition
CFDTD	Conformal finite difference time domain
FDTD	Finite difference time domain
PML	Perfectly matched layer

LIST OF FIGURES

Figure 2.1 Geometry of the wedge scattering problem (SSI: Single Side illumination, DSI: Double Side Illumination)	4
Figure 2.2 The front panel of the EM virtual tool WedgeGUI.....	14
Figure 2.3 Basic flow chart of WedgeGUI.....	14
Figure 2.4 Example scenario and output of WedgeGUI: Diffracted fields vs. angle for HBC ($\alpha = 350^\circ$, $\varphi_0 = 45^\circ$, $f = 30$ MHz, $r = 50$ m, $kr = 31.4159$). Curves belong to Exact, PTD, UTD, and PE models.....	15
Figure 2.5 Example scenario and the output of WedgeGUI: Total fields vs. angle for SBC ($\alpha = 330^\circ$, $\varphi_0 = 70^\circ$, $f = 30$ MHz, $r = 50$ m, $kr = 31.4159$). Curves belong to Exact, PO, and PTD models.....	16
Figure 2.6 Example scenario and the output of WedgeGUI: Diffracted fields vs. angle for HBC ($\alpha = 250^\circ$, $\varphi_0 = 150^\circ$, $f = 30$ MHz, $r = 50$ m, $kr = 31.4159$). Curves belong to Exact, PTD, and UTD models.	16
Figure 2.7 Diffracted fields vs. angle for (Left) SBC, (Right) HBC computed with Exact and UTD Models ($\alpha = 240^\circ$, $\varphi_0 = 110^\circ$, $f = 30$ MHz, $r = 50$ m, $kr = 31.4159$)	17
Figure 2.8 Total fields vs. angle for (Left) SBC, (Right) HBC computed with Exact and UTD models ($\alpha = 240^\circ$, $\varphi_0 = 110^\circ$, $f = 30$ MHz, $r = 50$ m, $kr = 31.4159$)	17
Figure 2.9 Diffraction coefficients vs. (Top) Frequency, (Bottom) Range for the plane wave illumination and SBC ($\alpha = 350^\circ$, $\varphi_0 = 60^\circ$, $f = 30$ MHz).....	18
Figure 3.1 Yee Cell.....	22
Figure 3.2 FDTD Algorithm.....	26
Figure 3.3 FDTD cell for TE_z mode	28
Figure 3.4 FDTD cell for TM_z mode	28
Figure 3.5 vp/vp versus ϕ for $\Delta t = \Delta/2vp$	33
Figure 3.6 vp/vp versus ϕ for $\Delta t = \Delta/2vp$	33
Figure 3.7 Plane wave incident on a lossy medium.....	36
Figure 3.8 Placement of PML in computational domain.....	40
Figure 3.9 TM_z FDTD simulation snapshot at $t = 20\Delta t$	51
Figure 3.10 TM_z FDTD simulation snapshot at $t = 150\Delta t$	52

Figure 3.11 TM_z FDTD simulation snapshot at $t = 300\Delta t$	52
Figure 3.12 Staircase modeling missile radome	54
Figure 3.13 Modified Faraday loop in Dey-Mittra technique	54
Figure 3.14 Dey-Mittra conformal FDTD scenarios	55
Figure 3.15 Comparison of Dey-Mittra conformal technique (a) and Staircase approximation (b)	56
Figure 3.16 Multi-step FDTD-based diffraction approach: (a) The wedge scenario, (b) Infinite-plane problem, (c) Free-space scenario	57
Figure 3.17 Front panel of WEDGE FDTD software.....	59
Figure 3.18 Total field, Diffracted field simulation results for TM_z mode.....	60
Figure 3.19 Total field, Diffracted field simulation results for TE_z mode.....	60

1 INTRODUCTION

The phenomena of electricity and magnetism were first noticed around 600 B.C. in ancient Greece. A piece of amber rubbed with a cloth was found to attract light objects, and pieces of a magnetic core were found to attract small iron objects. They are examples of static electric and magnetic fields respectively. In 19th century, experiments made by Faraday and Ampere showed that changing magnetic field induces a changing electric field and vice-versa—the two are linked. These changing fields form electromagnetic waves which propagate in all environments. Light, microwaves, radio and TV signals are all kinds of electromagnetic waves.

When the electromagnetic wave hits a material object, time varying polarization currents occur. This time-varying polarization currents create an additional electromagnetic field which is known as scattered field and propagates into both material and its surrounding space. Scattered fields are used to identify objects at a distance. For this reason, they are important for military, biomedical, aviation and mining applications. Extensive study of scattered fields leads to many discoveries in our lives such as stealth aircrafts, cancer detection systems. Scattered field which encloses reflected field, refracted field and diffracted field, can be analyzed via using analytical techniques such as geometric optics(GO), physical theory of diffraction(PTD), physical optics(PO), exact series and exact integral, for regular geometries.

On the other hand, the exact analytical solutions for scattering, radiation and wave guiding problems are rarely available or hard to obtain, for the irregular geometries which are found in actual devices. Several numerical techniques such as FDTD, Method of Moments, Finite Element Method, are emerged to overcome these difficulties. Improvement of the computer storage and increment of processor speeds enables us to use such numerical techniques more efficiently and accurately to obtain solutions of Maxwell's equations.

Through the numerical methods, FDTD is easy to use and powerful method for obtaining numerical solutions of Maxwell's equations in time domain as well as frequency domain via fast Fourier Transform (FFT). FDTD is based on solving differential form of

Maxwell's equations via central differences. Because of being time domain method, it makes possible to observe electromagnetic wave step by step.

1.1 Outline of the Thesis

This thesis is organized as follows: In Chapter 2, we review the analytical methods used for analyzing scattered fields for non-penetrable wedge geometry [1]. After introducing the general background, we introduce WEDGE GUI which is a novel matlab based tool developed to compare different analytical results obtained from plane wave or line source illumination of wedge type obstacle.

Chapter 3 gives detailed explanation about the application of FDTD method to obtain numerical solutions of Maxwell's equations for non-penetrable wedge type geometry. Modeling issues are also addressed in this chapter and alternative schemes are discussed to reduce numerical errors. At the end of the chapter, we introduce another novel matlab based tool WEDGE FDTD GUI which is 2D electromagnetic simulator based on FDTD method and developed to compare numerical results with analytical ones.

Although each chapter has its own concluding section, we summarize our results in chapter 4. It concludes this dissertation with a summary of the methods applied to obtain scattered fields and the future directions of our research.

Source codes of the developed programs are found in the CD given with this dissertation.

2 ANALYTICAL METHODS

2.1 Introduction

Electromagnetic (EM) wave scattering has been substantially investigated for many decades and just reviewed with a tutorial in [1] on the canonical, two-dimensional (2D) wedge problem. Numerical difficulties of various analytical models based on complex integration as well as series summation are also discussed in details in [2]. Comparisons against numerical techniques such as the Finite-Difference Time-Domain (FDTD) method are given in [3]. In all these studies, wave pieces like *reflection*, *refraction*, and *diffraction* which are the components of scattering are re-visited through analytical exact as well as High Frequency Asymptotic (HFA) methods, such as Geometrical Optics (GO), Geometrical Theory of Diffraction (GTD), its uniform extension Uniform Theory of Diffraction (UTD), Physical Optics (PO), Physical Theory of Diffraction (PTD), Elementary Edge Waves (EEW), and Parabolic Equation (PE) methods [4-20].

In this section, first, the problem is posted briefly and critical wave regions are outlined. Then, mathematical equations for both plane wave and line source illuminations are presented for the sake of completeness. There are many different forms of these models, but the ones presented here are numerically the most efficient ones. Finally, the virtual tool WedgeGUI is discussed together with some examples.

The non-penetrable wedge diffraction problem is canonical and plays a fundamental role in the construction of HFA techniques as well as for the numerical tests. The exact solution to this scattering problem was first found by Sommerfeld [4] in the particular case of a half-plane. For the wedge with an arbitrary angle between its faces, the solution was obtained by Macdonald [5] and later on by Sommerfeld who developed the method of branched wave functions [6].

The 2D wedge scattering scenario is pictured in figure 1. The semi-infinite wedge with PEC boundaries is located in vacuum. The polar coordinates are used throughout this section. The z-axis is aligned along the edge of the wedge. The angle φ_0 is measured from the top face of the wedge. The exterior angle of the wedge equals α . The wedge is

illuminated by a Line Source (LS) at a distance from a direction. In other words, source and observation points are given by (r_0, φ_0) and (r, φ) , respectively.

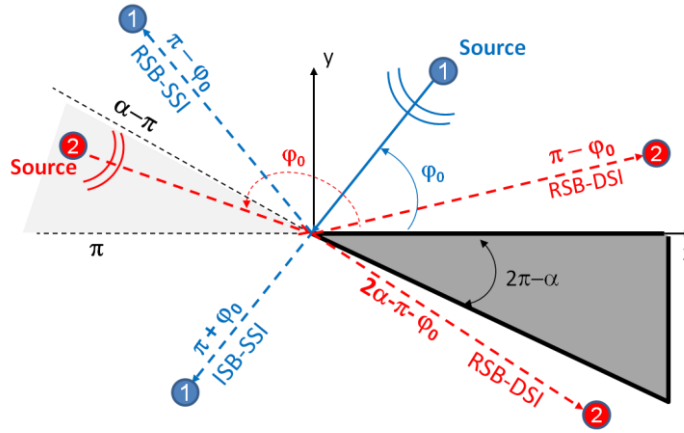


Figure 2.1 Geometry of the wedge scattering problem (SSI: Single Side illumination, DSI: Double Side Illumination)

The scenario for the LS-1 ($0 < \varphi_0 < \pi$) belongs to the Single Side Illumination (SSI) where the top face is always illuminated. In this case (i.e., for the SSI), the 2D scattering plane around the wedge may be divided into three regions in terms of critical wave phenomena occurred there. In Region-I ($0 \leq \varphi < \pi - \varphi_0$), all the field components – incident field, reflected field and diffracted field – exist. The angle $\varphi = \pi - \varphi_0$ is the limiting boundary of reflected fields and Region I (Reflection Shadow Boundary - RSB).

In Region-II ($\pi - \varphi_0 \leq \varphi \leq \pi + \varphi_0$) only incident and diffracted fields exist. The angle $\varphi = \pi + \varphi_0$ is the limiting boundary of the incident field and Region-II (Incident Shadow Boundary - ISB). In Region-III (i.e., in the shadow region, $+\varphi_0 \leq \varphi \leq \alpha$) only diffracted fields exist.

The scenario for the LS-2 ($\alpha - \pi < \varphi_0 < \pi$) belongs to the Double Side Illumination (DSI) where both faces are always illuminated. In this case, the 2D scattering plane around the wedge may also be divided into three regions. In Region-I ($0 \leq \varphi < \pi - \varphi_0$), all the field components – incident field, reflected fields from the top face, and diffracted field – exist. The angle $\varphi = \pi - \varphi_0$ is the limiting boundary and called Reflection Shadow Boundary–RSB. Similarly, in Region-III ($2\alpha - \pi - \varphi_0 \leq \varphi < \alpha$), all the field components – incident field, reflected fields from the bottom face, and diffracted field – exist. The angle $\varphi = 2\alpha - \pi - \varphi_0$ is also a RSB. The region between these two (i.e.,

Region-II; $\pi - \varphi_0 \leq \varphi < 2\alpha - \pi - \varphi_0$) contains no reflected fields and only incident and diffracted fields exist. In summary, both incident and diffracted fields exist everywhere, but reflected fields exist only in Region-1 and Region-3. Except the UTD formulations, the time dependence $e^{-(i\omega t)}$ is accepted in the section. The field outside the wedge satisfies the wave equation

$$\left(\frac{\partial^2}{\partial r^2} + \frac{1}{r} \frac{\partial}{\partial r} + \frac{1}{r^2} \frac{\partial^2}{\partial \varphi^2} + k^2 \right) u = \frac{I_0}{r} \delta(r - r_0) \delta(\varphi - \varphi_0) \quad (2.1)$$

and the boundary conditions (BC)

$$u_s = 0 \text{ or } \frac{\partial u_k}{\partial n} = 0 \text{ on } \varphi = 0, \alpha. \quad (2.2)$$

and the Sommerfeld's radiation condition at infinity:

$$\lim_{r \rightarrow \infty} \sqrt{kr} \left(\frac{du}{dr} - iku \right) = 0 \quad (2.3)$$

In the case of EM waves, these BCs are appropriate for the PEC wedge and function u_s represents the z-component of electric field intensity E_z (TM), while function u_h is the z-component of magnetic field intensity H_z (TE). In the case of acoustic waves, these conditions refer to acoustically soft (TM \rightarrow SBC) and hard (TE \rightarrow HBC) wedges, respectively.

2.2 Plane Wave Illumination and HFA Models

Mathematical equations of different models are included here for both Line source (LS) and Plane Wave (PW) illuminations. The PW models presented in this section are Exact by Series Summation, PO, PTD, UTD, and PE models.

2.2.1 Exact Solution by Series Summation

The total field solutions of the Helmholtz equation with SBC and HBC for both SSI and DSI are [11]:

$$u_{s,h} = u_0 [u(kr, \varphi - \varphi_0) \pm u(kr, \varphi + \varphi_0)] \quad (2.4)$$

where

$$u(kr, \Psi) = \frac{2\pi}{\alpha} \sum_{l=0}^{\infty} \epsilon_l e^{-i\left(\frac{\pi}{2}\right)v_l} J_{v_l}(kr) \cos(v_l \Psi) \quad (2.5)$$

$$u_0 = \frac{1}{4i} I_0 H_0^{(1)}(kr_0) \quad (2.6)$$

Here, $v_l = l\pi/a$ and $\epsilon_0 = 1/2$, $\epsilon_1 = \epsilon_2 = \epsilon_3 = \dots = 1$. The diffracted fields $u_s^{d,exact}$ and $u_h^{d,exact}$ can be calculated by subtracting suitable components (i.e., incident and/or reflected fields) from equation 2.4 in different regions as:

$$u_{s,h}^{d,Exact}/u_0 = u_{s,h}^{t,Exact}/u_0 - u_{s,h}^{GO} \quad (2.7)$$

where, for SSI ($0 < \varphi_0 < \alpha - \pi$)

$$u_{s,h}^{GO} = \begin{cases} e^{-ikrcos(\varphi-\varphi_0)} \pm e^{-ikrcos(\varphi+\varphi_0)} & 0 \leq \varphi < \pi - \varphi_0 \\ e^{-ikrcos(\varphi-\varphi_0)} & \pi - \varphi_0 \leq \varphi < \pi + \varphi_0 \\ 0 & \pi + \varphi_0 \leq \varphi \leq \alpha \end{cases} \quad (2.8)$$

and for DSI ($\alpha - \pi < \varphi_0 < \pi$)

$$u_{s,h}^{GO} = \begin{cases} e^{-ikrcos(\varphi-\varphi_0)} \pm e^{-ikrcos(\varphi+\varphi_0)} & 0 \leq \varphi < \pi - \varphi_0 \\ e^{-jkracos(\varphi-\varphi_0)} & \pi - \varphi_0 \leq \varphi < 2\alpha - \pi - \varphi_0 \\ 0 & 2\alpha - \pi - \varphi_0 \leq \varphi \leq \alpha \end{cases} \quad (2.9)$$

2.2.2 The Physical Optics (PO) Solution

The diffracted fields for the PO model (i.e., the uniform part of the surface currents) are given as [11]:

For SSI ($0 < \varphi_0 < \alpha - \pi$):

$$u_{s,h}^{d,PO}/u_0 = v_{s,h}^0(kr, \varphi, \varphi_0) \quad (2.10)$$

and, for DSI ($\alpha - \pi < \varphi_0 < \pi$):

$$u_{s,h}^{d,PO}/u_0 = v_{s,h}^0(kr, \varphi, \varphi_0) + v_{s,h}^0(kr, \alpha - \varphi, \alpha - \varphi_0) \quad (2.11)$$

where

$$v_s^0(kr, \varphi, \varphi_0) = \frac{1}{\pi\sqrt{2}} e^{i(kr+\frac{\pi}{4})} \int_{-\infty}^{\infty} e^{-krs^2} \left[\frac{1}{2} \cot \frac{\zeta + \Psi_1 - \pi}{2} - \frac{1}{2} \csc \frac{\zeta + \Psi_1 - \pi}{2} - \frac{1}{2} \cot \frac{\zeta + \Psi_2 - \pi}{2} + \frac{1}{2} \csc \frac{\zeta + \Psi_2 - \pi}{2} \right] \frac{ds}{\cos \frac{\zeta}{2}} \quad (2.12)$$

$$- e^{ikr \cos(\Psi_1)} \frac{e^{-\frac{i\pi}{4}}}{\sqrt{\pi}} \int_{\sqrt{2kr} \frac{\cos \Psi_1}{2}}^{\infty \frac{\cos \Psi_1}{2}} e^{ix^2} dx + e^{-ikr \cos(\Psi_2)} \frac{e^{-\frac{i\pi}{4}}}{\sqrt{\pi}} \int_{\sqrt{2kr} \cos(\frac{\Psi_2}{2})}^{\infty \cos(\frac{\Psi_2}{2})} e^{ix^2} dx$$

$$v_h^0(kr, \varphi, \varphi_0) = \frac{1}{\pi\sqrt{2}} e^{i(kr+\frac{\pi}{4})} \int_{-\infty}^{\infty} e^{-krs^2} \left[\frac{1}{2} \cot \frac{\zeta + \Psi_1 - \pi}{2} - \frac{1}{2} \csc \frac{\zeta + \Psi_1 - \pi}{2} + \frac{1}{2} \cot \frac{\zeta + \Psi_2 - \pi}{2} - \frac{1}{2} \csc \frac{\zeta + \Psi_2 - \pi}{2} \right] \frac{ds}{\cos \frac{\zeta}{2}} \quad (2.13)$$

$$- e^{ikr \cos(\Psi_1)} \frac{e^{-\frac{i\pi}{4}}}{\sqrt{\pi}} \int_{\sqrt{2kr} \frac{\cos \Psi_1}{2}}^{\infty \frac{\cos \Psi_1}{2}} e^{ix^2} dx + e^{-ikr \cos(\Psi_2)} \frac{e^{-\frac{i\pi}{4}}}{\sqrt{\pi}} \int_{\sqrt{2kr} \cos(\frac{\Psi_2}{2})}^{\infty \cos(\frac{\Psi_2}{2})} e^{ix^2} dx$$

Here, $\Psi_1 = \varphi - \varphi_0$ and $\Psi_2 = \varphi + \varphi_0$. The total fields, in these cases, can be obtained via

$$u_{s,h}^{t,PO} / u_0 = \frac{u_{s,h}^{d,PO}}{u_0} + u_{s,h}^{GO} \quad (2.14)$$

with the same GO solutions given in equations 2.8 and 2.9.

2.2.3 The PTD Solution

The PO proceeds from the hypothesis that a surface current on the illuminated side of a scattering object is determined by GO. This hypothesis is acceptable in the case of smooth objects whose radii of curvature are large compared to the wavelength; however, it neither satisfies the *reciprocity principle* nor the *boundary conditions* (BC). The PO also fails to predict depolarization of the diffracted field. The PTD improves PO by taking into account non-uniform surface currents and concentrates near edges. The PTD model is given as [11]:

$$u_{s,h}^{d,PTD} / u_0 = v_{s,h}^{(0)} + \frac{e^{i(kr+\frac{\pi}{4})}}{\sqrt{2\pi kr}} f_{s,h}^{(1)}(\varphi, \varphi_0, \alpha) \quad (2.15)$$

where

$$f_s^{(1)}(\varphi, \varphi_0, \alpha) = f_s(\varphi, \varphi_0, \alpha) - f_s^{(0)}(\varphi, \varphi_0, \alpha) \quad (2.16)$$

$$f_h^{(1)}(\varphi, \varphi_0, \alpha) = f_h(\varphi, \varphi_0, \alpha) - f_h^{(0)}(\varphi, \varphi_0, \alpha) \quad (2.17)$$

$$f_s(\varphi, \varphi_0, \alpha) = \frac{1}{2n} \left[\cot \frac{\pi - \varphi - \varphi_0}{2n} + \frac{\cot(\pi + \varphi + \varphi_0)}{2n} - \cot \frac{\pi - \varphi + \varphi_0}{2n} - \cot \frac{\pi + \varphi - \varphi_0}{2n} \right] \quad (2.18)$$

$$f_h(\varphi, \varphi_0, \alpha) = -\frac{1}{2n} \left[\cot \frac{\pi - \varphi - \varphi_0}{2n} + \frac{\cot(\pi + \varphi + \varphi_0)}{2n} + \cot \frac{\pi - \varphi + \varphi_0}{2n} + \cot \frac{\pi + \varphi - \varphi_0}{2n} \right] \quad (2.19)$$

$$f_s^0(\varphi, \varphi_0, \alpha) = \frac{\sin \varphi}{\cos \varphi_0 + \cos \varphi} + \epsilon(\alpha - \varphi_0) \frac{\sin(\alpha - \varphi_0)}{\cos(\alpha - \varphi) + \cos(\alpha - \varphi_0)} \quad (2.20)$$

$$f_h^0(\varphi, \varphi_0, \alpha) = \frac{-\sin \varphi}{\cos \varphi_0 + \cos \varphi} + \epsilon(\alpha - \varphi_0) \frac{-\sin(\alpha - \varphi_0)}{\cos(\alpha - \varphi) + \cos(\alpha - \varphi_0)} \quad (2.21)$$

and

$$\epsilon(\varphi_0) = \begin{cases} 0 & \text{if } 0 < \varphi_0 < \alpha - \pi \\ 1 & \text{if } \alpha - \pi < \varphi_0 < \pi \end{cases} \quad (2.22)$$

Again, the total fields, in these cases, can be obtained via

$$u_{t,h}^{t,PTD}/u_0 = u_{s,h}^{(d,PTD)}/u_0 + u_{s,h}^{GO} \quad (2.23)$$

with the same GO solutions given in equations 2.8 and 2.9.

2.2.4 The UTD Solution

The UTD diffracted fields are in the form of

$$u_{s,h}^{d,UTD} = u_0 d_{s,h}^{UTD} \frac{e^{-jkr}}{\sqrt{r}} \quad (2.24)$$

where $u_0 = H_0^2(kr_0)$ and the time dependence is $e^{j\omega t}$. According to the UTD, the diffraction coefficients for SBC and HBCs with line source as follows [13]

$$\begin{aligned} & d_s^{UTD}(r, \varphi, \varphi_0, k) \\ &= -\frac{e^{-\frac{j\pi}{4}}}{2n\sqrt{2\pi k}} \left[\begin{aligned} & \cot\left(\frac{\pi - \xi^-}{2n}\right) F(kLg^+(\xi^-)) + \cot\left(\frac{\pi + \xi^-}{2n}\right) F(kLg^-(\xi^-)) \\ & - \cot\left(\frac{\pi - \xi^+}{2n}\right) F(kLg^+(\xi^+)) - \cot\left(\frac{\pi + \xi^+}{2n}\right) F(kLg^-(\xi^+)) \end{aligned} \right] \end{aligned} \quad (2.25)$$

$$\begin{aligned} & d_h^{UTD}(r, \varphi, \varphi_0, k) \\ &= -\frac{e^{-\frac{j\pi}{4}}}{2n\sqrt{2\pi k}} \left[\begin{aligned} & \cot\left(\frac{\pi - \xi^-}{2n}\right) F(kLg^+(\xi^-)) + \cot\left(\frac{\pi + \xi^-}{2n}\right) F(kLg^-(\xi^-)) \\ & + \cot\left(\frac{\pi - \xi^+}{2n}\right) F(kLg^+(\xi^+)) + \cot\left(\frac{\pi + \xi^+}{2n}\right) F(kLg^-(\xi^+)) \end{aligned} \right] \end{aligned} \quad (2.26)$$

where $\xi^+ = \varphi + \varphi_0$, $\xi^- = \varphi - \varphi_0$ and $F(x)$ is the Fresnel function given as

$$F(x) = 2j\sqrt{x}e^{jx} \int_{\sqrt{x}}^{\infty} e^{-(j\tau^2)} d\tau \quad (2.27)$$

and L, g^\pm are determined as in [9]:

$$L = r, \quad g^\pm(\xi) = 2 \cos^2 \frac{2\pi n N^\pm - \xi}{2}, \quad N^\pm = \frac{\pm\pi + \xi}{2n\pi} \quad (2.28)$$

Here, N^\pm are the integers which most nearly satisfy the last equation given in equation 2.28. Note that the cotangent functions in equations 2.25 and 2.26 become singular at the ISB and RSB and are replaced as [13]:

$$\cot \frac{\pi \pm \beta}{2n} F(kLg^\pm(\xi)) n \left[\sqrt{2\pi k L} \operatorname{sgn}(\epsilon) - 2kL\epsilon e^{-\frac{j\pi}{4}} \right] e^{-\frac{j\pi}{4}} \quad (2.29)$$

for small ϵ . This term is finite but discontinuous at the ISB and RSB and compensates the discontinuities of the incident or reflected fields at these boundaries. The UTD based total fields are then obtained by adding the GO fields appropriately:

Again, the total fields, in these cases, can be obtained via

$$u_{s,h}^{t,UTD}/u_0 = u_{s,h}^{d,UTD}/u_0 + u_{s,h}^{GO} \quad (2.30)$$

with the GO solutions given as for SSI ($0 < \varphi_0 < \alpha - \pi$)

$$u_{s,h}^{GO} = \begin{cases} e^{-ikrcos(\varphi-\varphi_0)} \pm e^{-ikrcos(\varphi+\varphi_0)} & 0 \leq \varphi < \pi - \varphi_0 \\ e^{-ikrcos(\varphi-\varphi_0)} & \pi - \varphi_0 \leq \varphi < \pi + \varphi_0 \\ 0 & \pi + \varphi_0 \leq \varphi \leq \alpha \end{cases} \quad (2.31)$$

and for DSI ($\alpha - \pi < \varphi_0 < \pi$)

$$u_{s,h}^{GO} = \begin{cases} e^{-ikrcos(\varphi-\varphi_0)} \pm e^{-ikrcos(\varphi+\varphi_0)} & 0 \leq \varphi < \pi - \varphi_0 \\ e^{-jkrcos(\varphi-\varphi_0)} & \pi - \varphi_0 \leq \varphi < 2\alpha - \pi - \varphi_0 \\ 0 & 2\alpha - \pi - \varphi_0 \leq \varphi \leq \alpha \end{cases} \quad (2.32)$$

Note that, the UTD formulas are exactly the same for the line source excitation, except $L = r$ in is replaces with $L = r r_0/(r + r_0)$.

2.2.5 The Parabolic Equation (PE) Solution

As shown in [10] the method of Parabolic Equation (PE) provides a correct first-order approximation to the diffracted field in the case when $kr \gg 1$ and $kr_0 \gg 1$.

$$u_{s,h}^{d,PE} = u_0 W_{s,h}(kr, \varphi, \varphi_0) \quad (2.33)$$

where

$$W_{sh}(kr, \varphi, \varphi_0) = \frac{e^{i(kr + \frac{\pi}{4})}}{\pi\sqrt{2}} [w(kr, \Psi_1) \pm w(kr, \Psi_2)] \quad (2.34)$$

$$w(kr, \Psi) = \int_{-\infty}^{\infty} \frac{\frac{1}{n} \sin\left(\frac{\pi}{n}\right) e^{-krs^2}}{\cos\left(\frac{\pi}{n}\right) - \cos\left(\frac{\eta + \Psi}{n}\right)} ds \quad (2.35)$$

with $\Psi_{1,2} = \varphi \pm \varphi_0$, $n = \alpha/\pi$, and $\eta = \sqrt{2}e^{-\frac{i\pi}{4}}s$. Again, the total fields, in these cases, can be obtained via

$$u_{s,h}^{t,PE}/u_0 = u_{s,h}^{d,PE}/u_0 + u_{sh}^{GO} \quad (2.36)$$

with the same GO solutions given in equations 2.8 and 2.9.

2.3 HFA Models under Line Source Excitations

Mathematical equations of the models Exact by Series, Exact by Integral, the UTD, and PE, Line source (LS) illumination are presented in this section. Note that, numerical results of these models match with the PW models given in the previous section when the source-to-tip distance is large as compared with the wavelength.

2.3.1 Exact Solution by Series Summations

The total field solutions of the Helmholtz equation with SBC and HBC for both SSI and DSI are [11]:

$$u_s^{t,Exact} = \begin{cases} \frac{4\pi}{\alpha} \sum_{l=1}^{\infty} J_{v_l}(kr) H_{v_l}^{(1)}(kr_0) \sin(v_l \varphi_0) \sin(v_l \varphi) \dots & r \leq r_0 \\ \frac{4\pi}{\alpha} \sum_{l=1}^{\infty} J_{v_l}(kr_0) H_{v_l}^{(1)}(kr) \sin(v_l \varphi_0) \sin(v_l \varphi) \dots & r \geq r_0 \end{cases} \quad (2.37)$$

$$u_h^{t,Exact} = \begin{cases} \frac{4\pi}{\alpha} \sum_{l=0}^{\infty} \epsilon_l J_{v_l}(kr) H_{v_l}^{(1)}(kr_0) \cos(v_l \varphi_0) \cos(v_l \varphi) \dots & r \leq r_0 \\ \frac{4\pi}{\alpha} \sum_{l=0}^{\infty} \epsilon_l J_{v_l}(kr_0) H_{v_l}^{(1)}(kr) \cos(v_l \varphi_0) \cos(v_l \varphi) \dots & r \geq r_0 \end{cases} \quad (2.38)$$

with the same u_0 given in equation 2.6. Normalized diffracted fields $u_{s,h}^{d,Exact}$ can be obtained by subtracting GO fields

$$u_{s,h}^{d,Exact}/u_0 = \left(u_{s,h}^{t,Exact} - \frac{I_0}{4i} u_{s,h}^{GO} \right) / u_0 \quad (2.39)$$

The GO field that under LS excitation is given as follows:

For SSI:

$$u_{s,h}^{GO} = \begin{cases} H_0^{(1)}(kR_1) \pm H_0^{(1)}(kR_2) & 0 \leq \varphi < \pi - \varphi_0 \\ H_0^{(1)}(kR_1) & \pi - \varphi_0 \leq \varphi < \pi + \varphi_0 \\ 0 & \pi + \varphi_0 \leq \varphi \leq \alpha \end{cases} \quad (2.40)$$

For DSI:

$$u_{s,h}^{GO} = \begin{cases} H_0^{(1)}(kR_1) \pm H_0^{(1)}(kR_2) & 0 \leq \varphi < \pi - \varphi_0 \\ H_0^{(1)}(kR_1) & \pi - \varphi_0 \leq \varphi < 2\alpha - \pi - \varphi_0 \\ H_0^{(1)}(kR_1) \pm H_0^{(1)}(kR_3) & 2\alpha - \pi - \varphi_0 \leq \varphi \leq \alpha \end{cases} \quad (2.41)$$

where (−) and (+) for SBC and HBC respectively, and

$$R_1 = \sqrt{r^2 + r_0^2 - 2rr_0 \cos(\varphi - \varphi_0)} \quad (2.42)$$

$$R_2 = \sqrt{r^2 + r_0^2 - 2rr_0 \cos(\varphi + \varphi_0)} \quad (2.43)$$

$$R_3 = \sqrt{r^2 + r_0^2 - 2rr_0 \cos(2\alpha - \varphi - \varphi_0)} \quad (2.44)$$

2.3.2 Exact Solution by Integral

Solutions for the line source illumination are also well known and presented by Bowman and Senior in Handbook [8] as

$$u_s^{d,BS} = \{V_d(-\pi - \varphi + \varphi_0) - V_d(\pi - \varphi + \varphi_0)\} - \{V_d(-\pi - \varphi - \varphi_0) - V_d(\pi - \varphi - \varphi_0)\} \quad (2.45)$$

$$u_s^{d,BS} = \{V_d(-\pi - \varphi + \varphi_0) - V_d(\pi - \varphi + \varphi_0)\} + \{V_d(-\pi - \varphi - \varphi_0) - V_d(\pi - \varphi - \varphi_0)\} \quad (2.46)$$

where

$$V_d(\beta) = \frac{1}{2\pi n} \int_0^\infty H_0^{(1)}[kR(it)] \frac{\sin(\beta/n)}{\cosh(t/n) - \cos(\beta/n)} dt \quad (2.47)$$

$n = \alpha/\pi$ and $R(\eta) = \sqrt{r^2 + r_0^2 + 2rr_0 \cos(\eta)}$. In this case, total fields are obtained by

adding the GO fields. Again, the total fields, in these cases, can be obtained via

$$u_{s,h}^{t,BM}/u_0 = (u_{s,h}^{d,BM} + u_{s,h}^{GO})/u_0 \quad (2.48)$$

with the same GO solutions given in equations 2.8 and 2.9.

2.3.3 The Parabolic Equation (PE) Solution

The PE solution under a line source illumination when $kr \gg 1$ and $kr_0 \gg 1$ can be listed as follows [10]:

$$u_{s,h}^{d,PE}/u_0 = W_{s,h}(k\rho, \varphi, \varphi_0); \quad \rho = \frac{rr_0}{r + r_0} \quad (2.49)$$

where

$$W_{s,h}(k\rho, \varphi, \varphi_0) = \frac{e^{i(k\rho + \frac{\pi}{4})}}{\pi\sqrt{2}} [w(k\rho, \Psi_1) \pm w(k\rho, \Psi_2)] \quad (2.50)$$

$$w(k\rho, \Psi) = \int_{-\infty}^{\infty} \frac{\frac{1}{n} \sin\left(\frac{\pi}{n}\right) e^{-k\rho s^2}}{\cos\left(\frac{\pi}{n}\right) - \cos\left(\frac{\eta + \Psi}{n}\right)} ds \quad (2.51)$$

with $\Psi_{1,2} = \varphi \pm \varphi_0$, $n = \alpha/\pi$, and $\eta = \sqrt{2}e^{-\frac{i\pi}{4}}s$. Again, the total fields, in these cases, can be obtained via

$$u_{s,h}^{t,PE}/u_0 = \left(u_{s,h}^{d,PE} + \frac{I_0}{4i} u_{s,h}^{GO} \right) / u_0 \quad (2.52)$$

with the same GO solutions are given in equations 2.8 and 2.9.

2.4 The WedgeGUI Virtual Tool and Some Examples

The Matlab-based simulation package WedgeGUI with the front panel displayed in figure 2.2, is prepared for the investigation of wedge diffraction in 2D with various HFA models. The panel is divided into three parts. The top block is reserved for the structure. The wedge figure is shown on the top right. The wedge exterior angle incident distance and angle are supplied on the top left. The user also selects either of the Soft and Hard boundary conditions and total and diffracted fields in this block. A pop-up menu allows the user to choose the type of the source: Plane wave excitation or cylindrical wave excitation. For

each source type the methods used in simulations are given with tick boxes. Multiple selection is possible. The flow chart of the virtual tool is given in figure 2. 3.

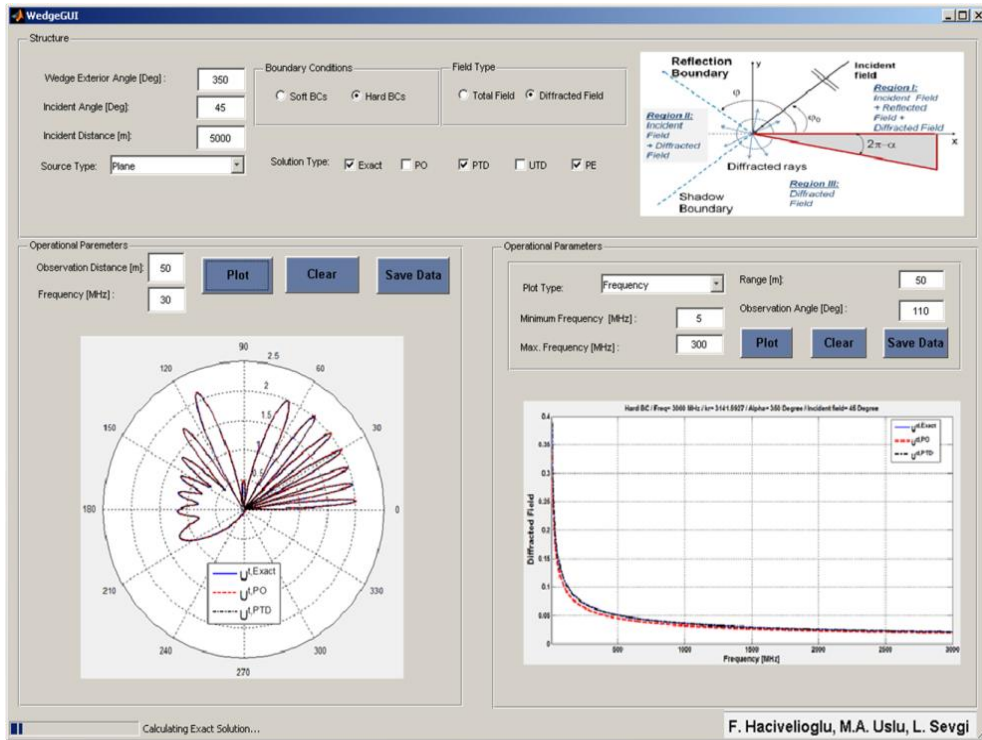


Figure 2.2 The front panel of the EM virtual tool WedgeGUI

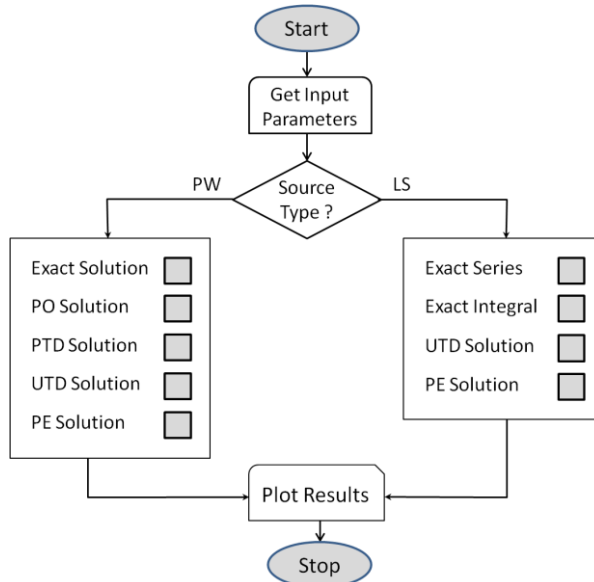


Figure 2.3 Basic flow chart of WedgeGUI

The area below the structure block is divided into two parts. On the left, the results are presented in terms of polar plots (i.e., fields vs. angle), on the right in terms of Cartesian plots (i.e., field vs. radial range or field vs. frequency). For the polar plots on the left block, one needs to specify frequency and radial distance from the tip. The rest is handled automatically once the Plot button is pressed and fields are calculated at N observation points equidistant from the tip located $\varphi = 2\pi/N$ apart. The progress bar on the bottom-left shows the status of the calculations. Figures 2.4-2.6 show example scenarios and simulation results.

The user may edit/modify the plot in another figure window. This is possible by clicking on the polar plot. Similarly, one can plot field vs. range or field vs. frequency on the right block. Clear button clears the plot for the next simulation and Save Data button records the data in a text file with the name given by the user. Table 1 lists a sample recorded data (partially) which belongs to the simulations presented in figure 2.6. Data recording is important because WedgeGUI do not run simulations for both SBC and HBC, or both total and diffracted fields at the same time. One needs to run WedgeGUI twice for the examples presented in figures 2.7-2.9.

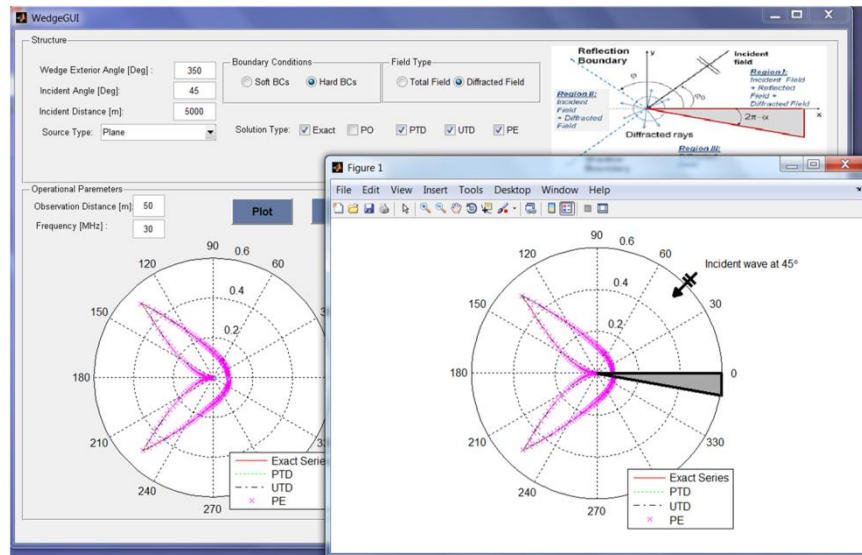


Figure 2.4 Example scenario and output of WedgeGUI: Diffracted fields vs. angle for HBC ($\alpha = 350^\circ$, $\varphi_0 = 45^\circ$, $f = 30$ MHz, $r = 50$ m, $kr = 31.4159$). Curves belong to Exact, PTD, UTD, and PE models

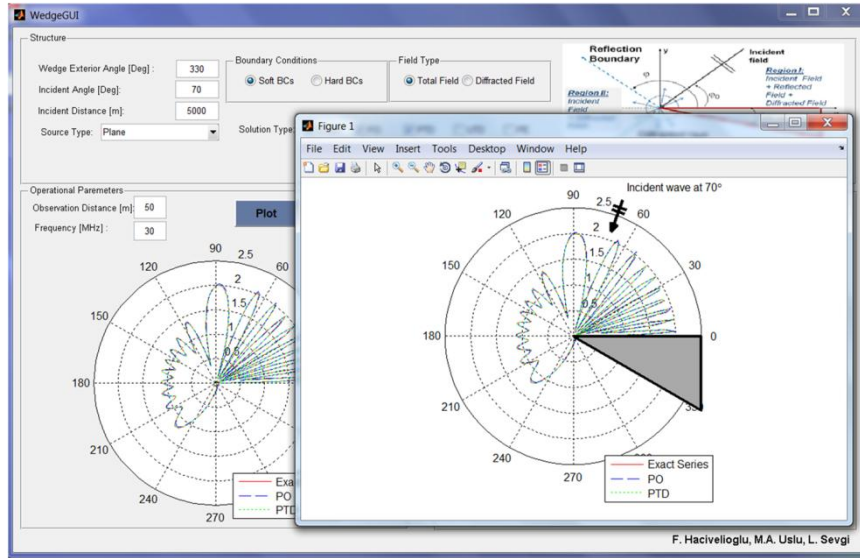


Figure 2.5 Example scenario and the output of WedgeGUI: Total fields vs. angle for SBC ($\alpha = 330^\circ$, $\varphi_0 = 70^\circ$, $f = 30$ MHz, $r = 50$ m, $kr = 31.4159$). Curves belong to Exact, PO, and PTD models.

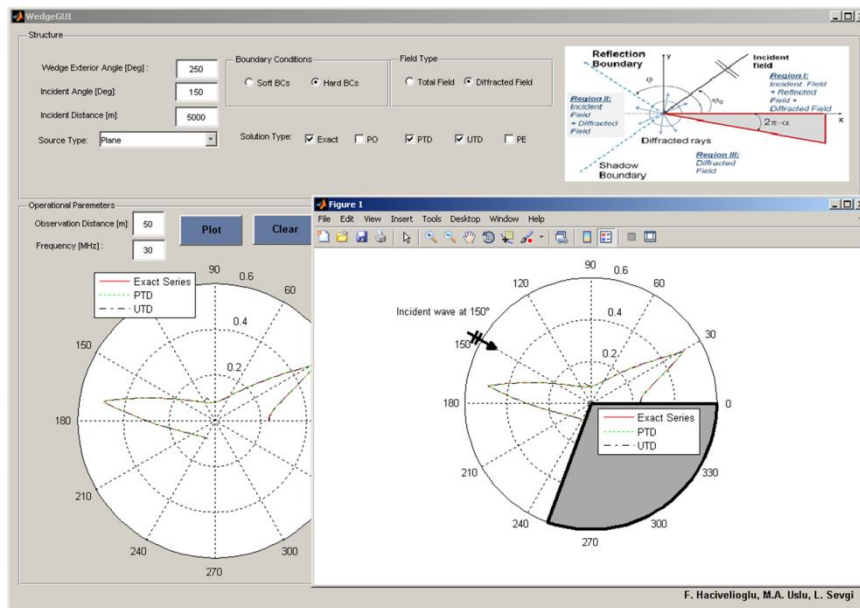


Figure 2.6 Example scenario and the output of WedgeGUI: Diffracted fields vs. angle for HBC ($\alpha = 250^\circ$, $\varphi_0 = 150^\circ$, $f = 30$ MHz, $r = 50$ m, $kr = 31.4159$). Curves belong to Exact, PTD, and UTD models.

Table 1. Sample recorded data for angle vs. diffracted fields.

Amplitude vs Angle, Created by WEDGE GUI Version 1.0

Angle[Degree]	Exact Series	PTD	UTD
0.000000e+000	0.000000e+000	0.000000e+000	0.000000e+000
1.330000e+000	5.4950027e-003	5.4851693e-003	5.4285868e-003
2.660000e+000	1.1015934e-002	1.0998098e-002	1.0908876e-002
3.990000e+000	1.6622216e-002	1.6597513e-002	1.6493445e-002
5.320000e+000	2.2373057e-002	2.2342250e-002	2.2236632e-002
6.650000e+000	2.8329854e-002	2.8292589e-002	2.8195433e-002
7.980000e+000	3.455510e-002	3.4511491e-002	3.4430417e-002
9.310000e+000	4.1117204e-002	4.1065763e-002	4.1006665e-002
1.064000e+001	4.8087060e-002	4.8027194e-002	4.7994723e-002
1.197000e+001	5.5543243e-002	5.5473639e-002	5.5471573e-002
1.330000e+001	6.3571012e-002	6.3490084e-002	6.3521588e-002
1.463000e+001	7.2263720e-002	7.2169651e-002	7.2237467e-002
1.596000e+001	8.1723727e-002	8.1614516e-002	8.1721102e-002
1.729000e+001	9.2063177e-002	9.1936713e-002	9.2084332e-002
1.862000e+001	1.0340459e-001	1.0325875e-001	1.0344952e-001
1.995000e+001	1.1588115e-001	1.1571393e-001	1.1594986e-001
2.128000e+001	1.2963667e-001	1.2944638e-001	1.2972932e-001
2.261000e+001	1.4466881e-001	1.4461046e-001	1.4494213e-001
2.394000e+001	1.6151492e-001	1.6136964e-001	1.6175153e-001
2.527000e+001	1.8011955e-001	1.7989450e-001	1.8032779e-001
2.660000e+001	2.0063371e-001	2.0035969e-001	2.0084517e-001
2.793000e+001	2.2323731e-001	2.2293967e-001	2.2347760e-001
2.926000e+001	2.4810853e-001	2.4780299e-001	2.4839293e-001
3.059000e+001	2.7533998e-001	2.7538568e-001	2.7531927e-001
3.192000e+001	3.0438172e-001	3.0435449e-001	3.045779e-001
3.325000e+001	3.3525666e-001	3.3525666e-001	3.3525666e-001
3.458000e+001	3.6845421e-001	3.6845421e-001	3.6845421e-001
3.591000e+001	4.04781607e-001	4.04781607e-001	4.04781607e-001
3.724000e+001	4.4436394e-001	4.4436394e-001	4.4436394e-001
3.857000e+001	4.87200150e-001	4.87200150e-001	4.87200150e-001
3.990000e+001	5.33462806e-001	5.33462806e-001	5.33462806e-001

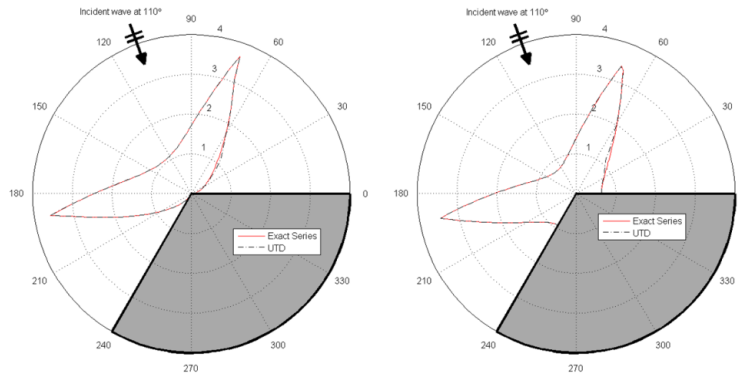


Figure 2.7 Diffracted fields vs. angle for (Left) SBC, (Right) HBC computed with Exact and UTD Models ($\alpha = 240^\circ, \varphi_0 = 110^\circ, f = 30 \text{ MHz}, r = 50 \text{ m}, kr = 31.4159$)

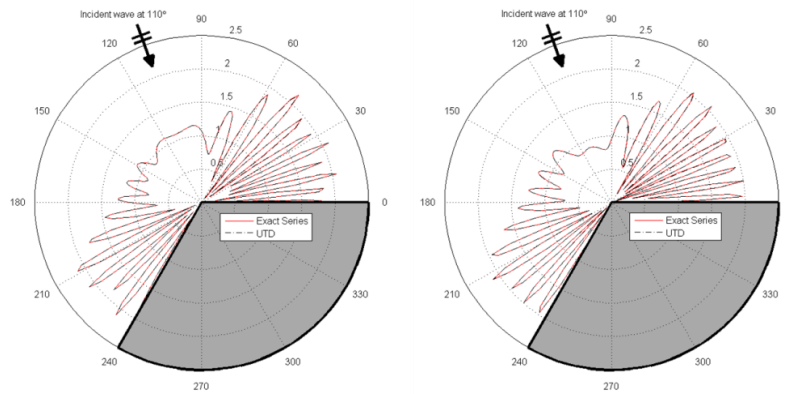


Figure 2.8 Total fields vs. angle for (Left) SBC, (Right) HBC computed with Exact and UTD models ($\alpha = 240^\circ, \varphi_0 = 110^\circ, f = 30 \text{ MHz}, r = 50 \text{ m}, kr = 31.4159$)

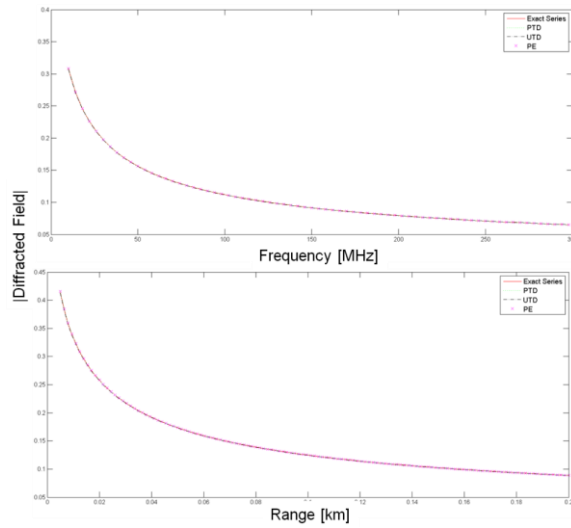


Figure 2.9 Diffraction coefficients vs. (Top) Frequency, (Bottom) Range for the plane wave illumination and SBC ($\alpha = 350^\circ$, $\varphi_0 = 60^\circ$, $f = 30$ MHz)

2.5 Conclusions

A MatLab-based virtual diffraction tool, WedgeGUI, is introduced. The WedgeGUI presents results of electromagnetic wave scattering from a wedge shaped object with Perfectly Electrical Conductor (PEC) boundaries under different structural as well as operational parameters. Various models under both line source and plane wave illuminations are included. Comparisons among Uniform Theory of Diffraction (UTD), Physical Optics (PO), Physical Theory of Diffraction (PTD), Parabolic Equation (PE) models through many scenarios and illustrations are possible. The WedgeGUI virtual tool can be used in many graduate and PhD level courses such as Advanced Electromagnetic Theory, High Frequency Asymptotic Methods in Electromagnetics, Diffraction Theory, etc.

3 FINITE DIFFERENCE TIME DOMAIN (FDTD) METHOD

3.1 Introduction

FDTD method is introduced by Yee in 1966 [21] is arguably the simplest of numerical methods used to solve electromagnetic problems. It is based on simple formulations which don't require complex asymptotic or Green's functions. Yee's idea was to divide simulation space into cells to form a grid and solve differential form of the Maxwell's equations around these cells by using second-order central differences. Although it is time domain based method, it can provide frequency domain responses via Fourier transform. FDTD has been used to solve various types of problems arises in our lives including scattering, radar cross section, cancer detection, cell phone radiation over human head and geological applications.

Since FDTD is based on discretizing time and simulation space, it is useful to explain numerical derivatives. Taylor series expansion of the multivariable function $f(x, t)$ around the specified time t_0 can be written as;

$$f(x, t) = f(x, t_0) + (t - t_0) \frac{\partial f(x, t_0)}{\partial t} + \frac{1}{2} (t - t_0)^2 \frac{\partial^2 f(x, t_0)}{\partial t^2} + \dots \quad (3.1)$$

If the function $f(x, t)$ is sampled in time with Δt intervals we can write equation 3.1 as follows

$$f(x, t_0 + \Delta t) = f(x, t_0) + (\Delta t) \frac{\partial f(x, t_0)}{\partial t} + \frac{1}{2} (\Delta t)^2 \frac{\partial^2 f(x, t_0)}{\partial t^2} + \dots \quad (3.2)$$

After rearranging terms we obtain:

$$\frac{\partial f(x, t_0)}{\partial t} = \frac{(f(x, t_0 + \Delta t) - f(x, t_0))}{\Delta t} - \frac{1}{2} \Delta t \frac{\partial^2 f(x, t_0)}{\partial t^2} - \dots \quad (3.3)$$

In a similar manner, the same expansion can be repeated for finding space derivative of the function. The terms in the Taylor series extends to infinity and due to the discrete nature of the computers, this expansion should be truncated after desired accuracy is obtained. As it

is seen by the equation (3.3) the other terms multiplied with the orders of Δt . According to truncation of terms there are several numerical derivative approximations. If we omit the terms which multiplied with the orders of Δt in equation 3.3, we obtain:

$$\frac{\partial f(x, t_0)}{\partial t} \approx \frac{(f(x, t_0 + \Delta t) - f(x, t_0))}{\Delta t} \quad (3.4)$$

This approximation is called first-order forward difference approximation of the derivative of the function $f(x, t_0)$. The term “first-order” comes from the fact that we omitted the terms multiplied with the orders of Δt starting from the first order in the equation (3.3). The term “forward” comes from the fact that, one forward time $f(x, t_0 + \Delta t)$ is used to evaluate derivative.

In kind, expansion of $f(x, t_0 - \Delta t)$ around the point t_0 gives

$$f(x, t_0 - \Delta t) = f(x, t_0) - (\Delta t) \frac{\partial f(x, t_0)}{\partial t} + \frac{1}{2} (\Delta t)^2 \frac{\partial^2 f(x, t_0)}{\partial t^2} - \dots \quad (3.5)$$

Leaving the first order derivative alone we have

$$\frac{\partial f(x, t_0)}{\partial t} = \frac{(f(x, t_0) - f(x, t_0 - \Delta t))}{\Delta t} + \frac{1}{2} \Delta t \frac{\partial^2 f(x, t_0)}{\partial t^2} - \dots \quad (3.6)$$

Neglecting the terms multiplied with the powers of Δt , we obtain the first-order backward approximation of the derivative of the function $f(x, t_0)$.

$$\frac{\partial f(x, t_0)}{\partial t} \approx \frac{(f(x, t_0) - f(x, t_0 - \Delta t))}{\Delta t} \quad (3.7)$$

The third way of obtaining a formula for an approximation of the derivative is obtained by averaging the forward and backward difference formulas such that

$$\begin{aligned} & f(x, t_0 + \Delta t) - f(x, t_0 - \Delta t) \\ &= 2\Delta t \frac{\partial f(x, t_0)}{\partial t} + \frac{1}{3} (\Delta t)^3 \frac{\partial^3 f(x, t_0)}{\partial t^3} - \dots \end{aligned} \quad (3.8)$$

After rearranging terms, we obtain

$$\frac{\partial f(x, t_0)}{\partial t} = \frac{f(x, t_0 + \Delta t) - f(x, t_0 - \Delta t)}{2\Delta t} - \frac{(\Delta t)^2}{6} \frac{\partial^3 f(x, t_0)}{\partial t^3} + \dots \quad (3.9)$$

In this case there is no term multiplied with first order of Δt . Neglecting the terms multiplied with the powers of Δt gives second-order centered difference approximation.

$$\frac{\partial f(x, t_0)}{\partial t} \approx \frac{f(x, t_0 + \Delta t) - f(x, t_0 - \Delta t)}{2\Delta t} \quad (3.10)$$

The error introduced by using this approximation is less than the first-order forward or backward approximations. For example, if the time step Δt is reduced to half of its value the error reduced by a factor of four.

3.2 3D FDTD Algorithm

Yee's algorithm approximates the derivatives in the differential form of Maxwell's equations shown in equations 3.11 – 3.14 with second-order centered differences.

$$\nabla \cdot \mathbf{E} = \frac{\rho}{\epsilon_0} \quad (3.11)$$

$$\nabla \cdot \mathbf{H} = 0 \quad (3.12)$$

$$\nabla \times \mathbf{E} = -\frac{\partial \mathbf{B}}{\partial t} - \mathbf{M} \quad (3.13)$$

$$\nabla \times \mathbf{H} = \frac{\partial \mathbf{D}}{\partial t} + \mathbf{J} \quad (3.14)$$

where ∇ is $\frac{\partial}{\partial t} \mathbf{x} + \frac{\partial}{\partial t} \mathbf{y} + \frac{\partial}{\partial t} \mathbf{z}$.

The spatial positions of the field components have specific arrangement in the Yee cell as shown in figure 3.1. In this arrangement electric fields are placed at the centers of the edges of Yee cell and magnetic fields are placed at the center of the faces of the Yee cell. In other words, magnetic field components are surrounded by four electric field components and electric field components are surrounded by four magnetic field components. Instead, one can rearrange Yee cell so that location of the magnetic and electric field components are interchanged. But this arrangement has advantage because of the fact that boundary conditions imposed on electric field are more commonly encountered than those for magnetic field so placing the mesh boundaries so that they pass

through electric field vectors [22]. In addition to spatial arrangement, Yee assumed that the magnetic field components are calculated at half time steps slightly after electric field components. Therefore super script $n+1/2$ is used for magnetic fields to emphasize that they are calculated slightly after electric fields.

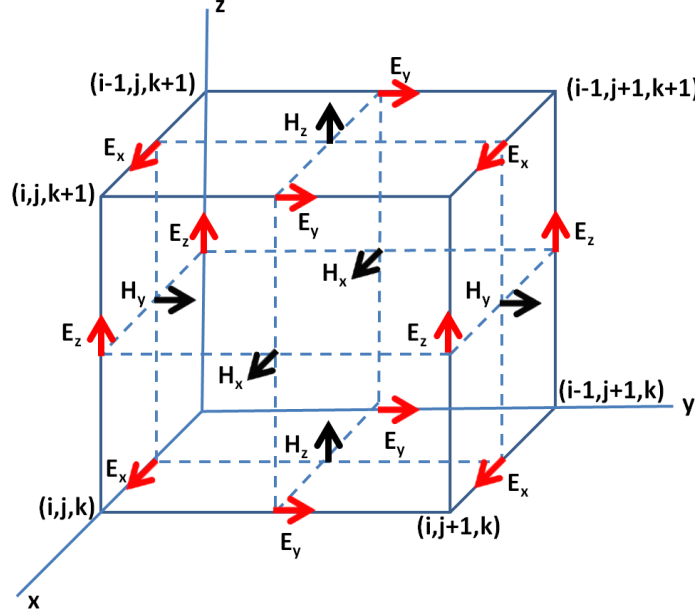


Figure 3.1 Yee Cell

Since we know the spatial locations of the field components, we are ready to discretize Maxwell's equations. We first start with writing open form of curl operator in equation 3.13.

$$\begin{aligned} \nabla \times \mathbf{E} &= \det \begin{vmatrix} \mathbf{i} & \mathbf{j} & \mathbf{k} \\ \frac{\partial}{\partial x} & \frac{\partial}{\partial y} & \frac{\partial}{\partial z} \\ E_x & E_y & E_z \end{vmatrix} \\ &= \left(\frac{\partial E_z}{\partial y} - \frac{\partial E_y}{\partial z} \right) \mathbf{i} + \left(\frac{\partial E_x}{\partial z} - \frac{\partial E_z}{\partial x} \right) \mathbf{j} + \left(\frac{\partial E_y}{\partial x} - \frac{\partial E_x}{\partial y} \right) \mathbf{k} \\ &= -\mu_0 \frac{\partial \mathbf{H}}{\partial t} \end{aligned} \tag{3.15}$$

Here we omitted the by omitting magnetic current density \mathbf{M} and electric current density \mathbf{J} . Writing $\mathbf{H} = \mathbf{i}H_x + \mathbf{j}H_y + \mathbf{k}H_z$ and equating with the left side of the equation 3.15 yields three coupled scalar equations:

$$\frac{\partial H_x}{\partial t} = \frac{1}{\mu} \left[\frac{\partial E_y}{\partial z} - \frac{\partial E_z}{\partial y} \right] \quad (3.16)$$

$$\frac{\partial H_y}{\partial t} = \frac{1}{\mu} \left[\frac{\partial E_z}{\partial x} - \frac{\partial E_x}{\partial z} \right] \quad (3.17)$$

$$\frac{\partial H_z}{\partial t} = \frac{1}{\mu} \left[\frac{\partial E_x}{\partial y} - \frac{\partial E_y}{\partial x} \right] \quad (3.18)$$

Repeating the same process for equation 3.14 we obtain:

$$\nabla \times \mathbf{H} = \det \begin{vmatrix} i & j & k \\ \frac{\partial}{\partial x} & \frac{\partial}{\partial y} & \frac{\partial}{\partial z} \\ H_x & H_y & H_z \end{vmatrix} \quad (3.19)$$

$$= \left(\frac{\partial H_z}{\partial y} - \frac{\partial H_y}{\partial z} \right) \vec{i} + \left(\frac{\partial H_x}{\partial z} - \frac{\partial H_z}{\partial x} \right) \vec{j} + \left(\frac{\partial H_y}{\partial x} - \frac{\partial H_x}{\partial y} \right) \vec{k} = \epsilon \frac{\partial \mathbf{E}}{\partial t}$$

In a similar manner, Writing $\mathbf{E} = \vec{i}E_x + \vec{j}E_y + \vec{k}E_z$ and equating with the left side of the equation 3.19 yields three coupled scalar equations:

$$\frac{\partial E_x}{\partial t} = \frac{1}{\epsilon} \left[\frac{\partial H_z}{\partial y} - \frac{\partial H_y}{\partial z} \right] \quad (3.20)$$

$$\frac{\partial E_y}{\partial t} = \frac{1}{\epsilon} \left[\frac{\partial H_x}{\partial z} - \frac{\partial H_z}{\partial x} \right] \quad (3.21)$$

$$\frac{\partial E_z}{\partial t} = \frac{1}{\epsilon} \left[\frac{\partial H_y}{\partial x} - \frac{\partial H_x}{\partial y} \right] \quad (3.22)$$

Referring to figure 3.1, we can approximate the derivatives of the equations 3.16 – 3.22 via second-order centered differences. Applying the second-order centered difference approximation to the time and space derivatives in equation 3.16 yields:

$$\begin{aligned}
& \frac{H_x|_{i,j+\frac{1}{2},k+\frac{1}{2}}^{n+\frac{1}{2}} - H_x|_{i,j+\frac{1}{2},k+\frac{1}{2}}^{n-\frac{1}{2}}}{2\Delta t} \\
&= \frac{1}{\mu_{i,j+\frac{1}{2},k+\frac{1}{2}}} \left[\frac{E_y|_{i,j+\frac{1}{2},k+1}^n - E_y|_{i,j+\frac{1}{2},k}^n}{2\Delta z} - \frac{E_z|_{i,j+1,k+\frac{1}{2}}^n - E_z|_{i,j,k+\frac{1}{2}}^n}{2\Delta y} \right]
\end{aligned} \tag{3.23}$$

Rearranging terms in equation 3.23, we obtain:

$$\begin{aligned}
& H_x|_{i,j+\frac{1}{2},k+\frac{1}{2}}^{n+\frac{1}{2}} = H_x|_{i,j+\frac{1}{2},k+\frac{1}{2}}^{n-\frac{1}{2}} \\
& + \frac{\Delta t}{\mu_{i,j+\frac{1}{2},k+\frac{1}{2}}} \left[\frac{E_y|_{i,j+\frac{1}{2},k+1}^n - E_y|_{i,j+\frac{1}{2},k}^n}{\Delta z} - \frac{E_z|_{i,j+1,k+\frac{1}{2}}^n - E_z|_{i,j,k+\frac{1}{2}}^n}{\Delta y} \right]
\end{aligned} \tag{3.24}$$

In equation 3.24 we have used compact form field components i.e. $H_x|_{i,j+\frac{1}{2},k+\frac{1}{2}}^{n+\frac{1}{2}} = H_x\left(i, j + \frac{1}{2}, k + \frac{1}{2}, n + \frac{1}{2}\right)$. Here, superscript n is used for time step and subscript i, j, k is used for spatial location. The remaining components are presented in the equations 3.25 – 3.30.

$$\begin{aligned}
& H_y|_{i+\frac{1}{2},j,k+\frac{1}{2}}^{n+\frac{1}{2}} = H_y|_{i+\frac{1}{2},j,k+\frac{1}{2}}^{n-\frac{1}{2}} \\
& + \frac{\Delta t}{\mu_{i+\frac{1}{2},j,k+\frac{1}{2}}} \left[\frac{E_z|_{i+1,j,k+\frac{1}{2}}^n - E_z|_{i,j,k+\frac{1}{2}}^n}{\Delta x} - \frac{E_x|_{i+\frac{1}{2},j,k+1}^n - E_x|_{i+\frac{1}{2},j,k}^n}{\Delta z} \right]
\end{aligned} \tag{3.25}$$

$$\begin{aligned}
& H_z|_{i+\frac{1}{2},j+\frac{1}{2},k}^{n+\frac{1}{2}} = H_z|_{i+\frac{1}{2},j+\frac{1}{2},k}^{n-\frac{1}{2}} \\
& + \frac{\Delta t}{\mu_{i+\frac{1}{2},j+\frac{1}{2},k}} \left[\frac{E_x|_{i+\frac{1}{2},j+1,k}^n - E_x|_{i+\frac{1}{2},j,k}^n}{\Delta y} - \frac{E_y|_{i+1,j+\frac{1}{2},k}^n - E_y|_{i,j+\frac{1}{2},k}^n}{\Delta x} \right]
\end{aligned} \tag{3.26}$$

$$\begin{aligned}
E_x|_{i+\frac{1}{2},j,k}^{n+1} &= E_x|_{i+\frac{1}{2},j,k}^n \\
&+ \frac{\Delta t}{\epsilon_{i+\frac{1}{2},j,k}} \left[\frac{H_z|_{i+\frac{1}{2},j+\frac{1}{2},k}^{n+\frac{1}{2}} - H_z|_{i+\frac{1}{2},j-\frac{1}{2},k}^{n+\frac{1}{2}}}{\Delta y} \right. \\
&\quad \left. - \frac{H_y|_{i+\frac{1}{2},k+\frac{1}{2}}^{n+\frac{1}{2}} - H_y|_{i+\frac{1}{2},k-\frac{1}{2}}^{n+\frac{1}{2}}}{\Delta z} \right]
\end{aligned} \tag{3.27}$$

$$\begin{aligned}
E_y|_{i,j+\frac{1}{2},k}^{n+1} &= E_y|_{i,j+\frac{1}{2},k}^n \\
&+ \frac{\Delta t}{\epsilon_{i,j+\frac{1}{2},k}} \left[\frac{H_x|_{i,j+\frac{1}{2},k+\frac{1}{2}}^{n+\frac{1}{2}} - H_x|_{i,j+\frac{1}{2},k-\frac{1}{2}}^{n+\frac{1}{2}}}{\Delta z} \right. \\
&\quad \left. - \frac{H_z|_{i+\frac{1}{2},j+\frac{1}{2},k}^{n+\frac{1}{2}} - H_z|_{i-\frac{1}{2},j+\frac{1}{2},k}^{n+\frac{1}{2}}}{\Delta x} \right]
\end{aligned} \tag{3.28}$$

$$\begin{aligned}
E_z|_{i,j,k+\frac{1}{2}}^{n+1} &= E_z|_{i,j,k+\frac{1}{2}}^n \\
&+ \frac{\Delta t}{\epsilon_{i,j,k+\frac{1}{2}}} \left[\frac{H_y|_{i+\frac{1}{2},j,k+\frac{1}{2}}^{n+\frac{1}{2}} - H_y|_{i-\frac{1}{2},j,k+\frac{1}{2}}^{n+\frac{1}{2}}}{\Delta x} \right. \\
&\quad \left. - \frac{H_x|_{i,j+\frac{1}{2},k+\frac{1}{2}}^{n+\frac{1}{2}} - H_x|_{i,j-\frac{1}{2},k+\frac{1}{2}}^{n+\frac{1}{2}}}{\Delta y} \right]
\end{aligned} \tag{3.29}$$

Time step is explicit in FDTD algorithm such that magnetic fields are calculated before/after the electric fields. So we can disregard half-time step superscript in the equations 3.24-3.29. On the other hand, spatial steps are implicit and we cannot use double

numbers as an array index in high-level programming languages. Hence, we can apply the following rules to solve half-step problem:

When it comes to calculating E values of i, j, k indexes then the indexes of the necessary H value follow this rule:

- When the H index has a $+1/2$ assume its value 0
- When the H index has a $-1/2$ assume its value -1

When it comes to calculating H values of i, j, k indexes then the indexes of the necessary E value follow this rule:

- When the H index has a $-1/2$ assume its value 0
- When the H index has a $+1/2$ assume its value +1

The complete FDTD algorithm is shown at figure 3.2.

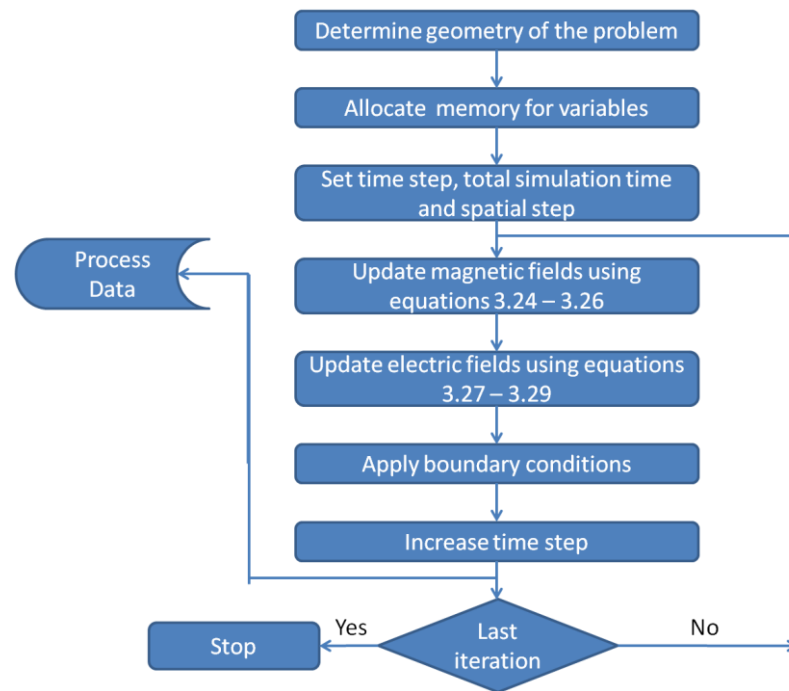


Figure 3.2 FDTD Algorithm

In this algorithm, selection of time step and spatial step requires specific attention as will be explained later.

3.3 Reduction to 2D TE and TM Modes

When both the structure being modeled and the excitation do not change with respect to specific direction, then the derivatives in Maxwell's curl equations (3.15 and 3.19) with respect to that direction vanish. For example, if the problem is z dimension independent we have:

$$\nabla \times \mathbf{E} = -\mu \frac{\partial \mathbf{H}}{\partial t} \rightarrow \begin{aligned} \frac{\partial H_x}{\partial t} &= -\frac{1}{\mu} \frac{\partial E_z}{\partial y} \\ \frac{\partial H_y}{\partial t} &= \frac{1}{\mu} \frac{\partial E_z}{\partial x} \\ \frac{\partial H_z}{\partial t} &= \frac{1}{\mu} \left[\frac{\partial E_x}{\partial y} - \frac{\partial E_y}{\partial x} \right] \end{aligned} \quad (3.30)$$

$$\nabla \times \mathbf{H} = \epsilon \frac{\partial \mathbf{E}}{\partial t} \rightarrow \begin{aligned} \frac{\partial E_x}{\partial t} &= \frac{1}{\epsilon} \frac{\partial H_z}{\partial y} \\ \frac{\partial E_y}{\partial t} &= -\frac{1}{\epsilon} \frac{\partial H_z}{\partial x} \\ \frac{\partial E_z}{\partial t} &= \frac{1}{\epsilon} \left[\frac{\partial H_y}{\partial x} - \frac{\partial H_x}{\partial y} \right] \end{aligned} \quad (3.31)$$

We can group equations 3.30 and 3.31 into two uncoupled sets called transverse magnetic (TM_z) and transverse electric (TE_z) modes as follows:

$$\begin{aligned} \frac{\partial H_x}{\partial t} &= -\frac{1}{\mu} \frac{\partial E_z}{\partial y} \\ \frac{\partial H_y}{\partial t} &= \frac{1}{\mu} \frac{\partial E_z}{\partial x} \\ \frac{\partial E_z}{\partial t} &= \frac{1}{\epsilon} \left[\frac{\partial H_y}{\partial x} - \frac{\partial H_x}{\partial y} \right] \end{aligned} \quad (3.32)$$

TM_z Mode

$$\begin{aligned} \frac{\partial E_x}{\partial t} &= \frac{1}{\epsilon} \frac{\partial H_z}{\partial y} \\ \frac{\partial E_y}{\partial t} &= -\frac{1}{\epsilon} \frac{\partial H_z}{\partial x} \\ \frac{\partial H_z}{\partial t} &= \frac{1}{\mu} \left[\frac{\partial E_x}{\partial y} - \frac{\partial E_y}{\partial x} \right] \end{aligned} \quad (3.33)$$

TE_z Mode

As it is seen by equations 3.32 and 3.33 TM_z and TE_z modes don't contain common field components and they are identified as which have a magnetic or electric field component in the axial (i.e. z) direction. Although the spatial locations of the field components are shown at figure 3.1, we present 2D slices obtained from figure 3.1 in figures 3.3 and 3.4 for clarity.

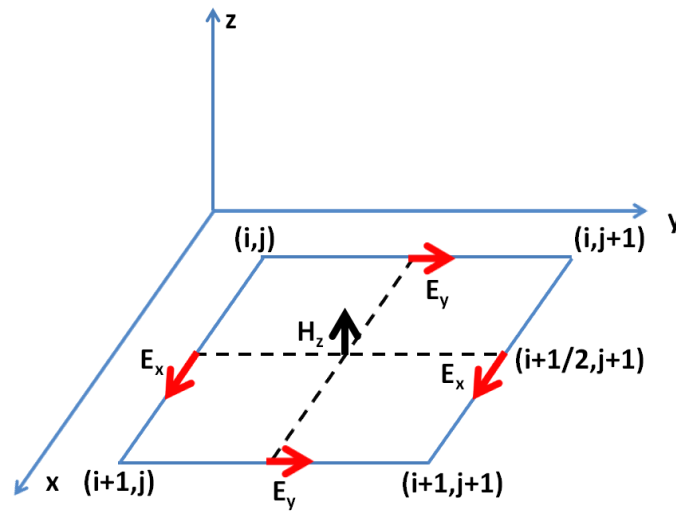


Figure 3.3 FDTD cell for TE_z mode

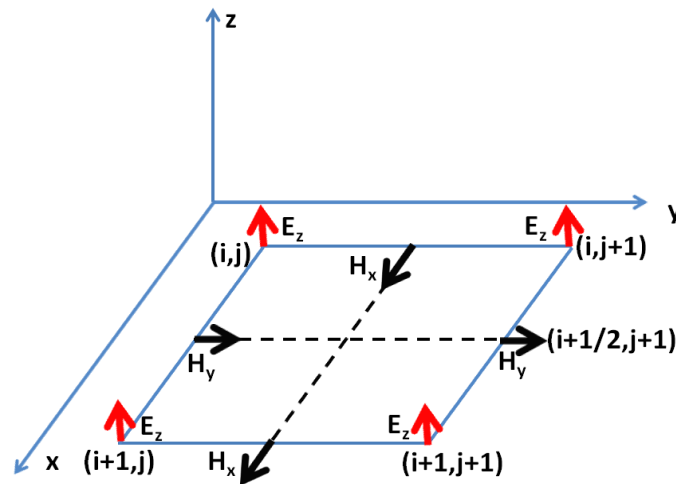


Figure 3.4 FDTD cell for TM_z mode

FDTD update equations for both TM_z and TE_z modes can be obtained by applying central difference approximation to the partial derivatives in the equations 3.32 and 3.33. For the sake of completeness we present them as follows:

TE_z Mode

$$H_z|_{i+\frac{1}{2},j+\frac{1}{2}}^{n+\frac{1}{2}} = H_z|_{i+\frac{1}{2},j+\frac{1}{2}}^{n-\frac{1}{2}} + \frac{\Delta t}{\mu_{i+\frac{1}{2},j+\frac{1}{2}}} \left[\frac{E_x|_{i+\frac{1}{2},j+1}^n - E_x|_{i+\frac{1}{2},j}^n}{\Delta y} - \frac{E_y|_{i+1,j+\frac{1}{2}}^n - E_y|_{i,j+\frac{1}{2}}^n}{\Delta x} \right] \quad (3.34)$$

$$E_x|_{i+\frac{1}{2},j}^{n+1} = E_x|_{i+\frac{1}{2},j}^n + \frac{\Delta t}{\epsilon_{i+\frac{1}{2},j}} \left[\frac{H_z|_{i+\frac{1}{2},j+\frac{1}{2}}^{n+\frac{1}{2}} - H_z|_{i+\frac{1}{2},j-\frac{1}{2}}^{n+\frac{1}{2}}}{\Delta y} \right] \quad (3.35)$$

$$E_y|_{i,j+\frac{1}{2}}^{n+1} = E_y|_{i,j+\frac{1}{2}}^n - \frac{\Delta t}{\epsilon_{i,j+\frac{1}{2}}} \left[\frac{H_z|_{i+\frac{1}{2},j+\frac{1}{2}}^{n+\frac{1}{2}} - H_z|_{i-\frac{1}{2},j+\frac{1}{2}}^{n+\frac{1}{2}}}{\Delta x} \right] \quad (3.36)$$

TM_z Mode

$$H_x|_{i,j+\frac{1}{2}}^{n+\frac{1}{2}} = H_x|_{i,j+\frac{1}{2}}^{n-\frac{1}{2}} - \frac{\Delta t}{\mu_{i,j+\frac{1}{2}}} \left[\frac{E_z|_{i,j+1}^n - E_z|_{i,j}^n}{\Delta y} \right] \quad (3.37)$$

$$H_y|_{i+\frac{1}{2},j}^{n+\frac{1}{2}} = H_y|_{i+\frac{1}{2},j}^{n-\frac{1}{2}} + \frac{\Delta t}{\mu_{i+\frac{1}{2},j}} \left[\frac{E_z|_{i+1,j}^n - E_z|_{i,j}^n}{\Delta x} \right] \quad (3.38)$$

$$E_z|_{i,j}^{n+1} = E_z|_{i,j}^n + \frac{\Delta t}{\epsilon_{i,j}} \left[\frac{H_y|_{i+\frac{1}{2},j}^{n+\frac{1}{2}} - H_y|_{i-\frac{1}{2},j}^{n+\frac{1}{2}}}{\Delta x} - \frac{H_x|_{i,j+\frac{1}{2}}^{n+\frac{1}{2}} - H_x|_{i,j-\frac{1}{2}}^{n+\frac{1}{2}}}{\Delta y} \right] \quad (3.39)$$

Most two-dimensional problems can be decomposed into TE and TM modes and can be solved separately because of the fact that they are uncoupled. The solution for the main problem is then obtained by summing the solutions of TE and TM modes.

3.4 Numerical Dispersion

Dispersion relation gives the relationship between wavelength and frequency. Dispersion occurs when the waves of different frequencies have different propagation velocities. For electromagnetic waves in vacuum, the frequency is proportional with wavelength λ and dispersion relation is given as:

$$\lambda = \frac{c}{f} \text{ or } \frac{\omega}{c} = k \quad (3.40)$$

In this chapter will try to find a dispersion relation for FDTD algorithm. For this purpose, we will analyze 2D FDTD algorithm for simplicity but the results can be extended to 3D FDTD algorithm easily. It is obvious that the following traveling-wave equations are the solutions of TM_z mode equations (3.37-3.39):

$$H_x|_{i,j}^n = H_{x0} e^{j(\omega n \Delta t - \bar{k}_x i \Delta x - \bar{k}_y j \Delta y)} \quad (3.41)$$

$$H_y|_{i,j}^n = H_{y0} e^{j(\omega n \Delta t - \bar{k}_x i \Delta x - \bar{k}_y j \Delta y)} \quad (3.42)$$

$$E_z|_{i,j}^n = E_{z0} e^{j(\omega n \Delta t - \bar{k}_x i \Delta x - \bar{k}_y j \Delta y)} \quad (3.43)$$

where \bar{k}_x and \bar{k}_y are the components of the numerical wavevector.

Using equations 3.41-3.43 in equation 3.37, we obtain the following equation.

$$\begin{aligned} & \left(H_{x0} e^{j(\omega n \Delta t)} e^{j(\omega \Delta t \frac{1}{2})} e^{-j(\bar{k}_x i \Delta x)} e^{-j(\bar{k}_y j \Delta y)} e^{-j(\bar{k}_y \frac{1}{2} \Delta y)} \right. \\ & \left. - H_{x0} e^{j(\omega n \Delta t)} e^{-j(\omega \frac{1}{2} \Delta t)} e^{-j(\bar{k}_x i \Delta x)} e^{-j(\bar{k}_y j \Delta y)} e^{-j(\bar{k}_y \frac{1}{2} \Delta y)} \right) \\ & / \Delta t \\ & = - \frac{1}{\mu \Delta y} (E_{z0} e^{j(\omega n \Delta t)} e^{-j(\bar{k}_x i \Delta x)} e^{-j(\bar{k}_y j \Delta y)} e^{-j(\bar{k}_y \Delta y)} \\ & \quad - E_{z0} e^{j(\omega n \Delta t)} e^{-j(\bar{k}_x i \Delta x)} e^{-j(\bar{k}_y j \Delta y)}) \end{aligned} \quad (3.44)$$

Dividing both sides of the equation by $e^{j(\omega n \Delta t)} e^{-j(\bar{k}_x i \Delta x)} e^{-j(\bar{k}_y (j + \frac{1}{2}) \Delta y)}$ we have

$$\begin{aligned}
H_{x0} & \left(\frac{e^{j(\omega\Delta t\frac{1}{2})} - e^{-j(\omega\Delta t\frac{1}{2})}}{\Delta t} \right) \\
& = -\frac{1}{\mu\Delta y} E_{z0} \left(e^{-j(\bar{k}_y\frac{1}{2}\Delta y)} - e^{+j(\bar{k}_y\frac{1}{2}\Delta y)} \right)
\end{aligned} \tag{3.45}$$

Additional simplification can be achieved by using Euler's formula:

$$H_{x0} = \frac{\Delta t}{\mu\Delta y} E_{z0} \frac{\sin\left(\frac{\bar{k}_y\Delta y}{2}\right)}{\sin\left(\frac{\omega\Delta t}{2}\right)} \tag{3.46}$$

In kind, the following equations can be derived for H_{y0} and E_{z0}

$$H_{y0} = -\frac{\Delta t}{\mu\Delta x} E_{z0} \frac{\sin\left(\frac{\bar{k}_x\Delta x}{2}\right)}{\sin\left(\frac{\omega\Delta t}{2}\right)} \tag{3.47}$$

$$E_{z0} \sin\left(\frac{\omega\Delta t}{2}\right) = \frac{\Delta t}{\epsilon} \left[\frac{H_{x0}}{\Delta y} \sin\left(\frac{\bar{k}_y\Delta y}{2}\right) - \frac{H_{y0}}{\Delta x} \sin\left(\frac{\bar{k}_x\Delta x}{2}\right) \right] \tag{3.48}$$

Upon substituting H_{x0} and H_{y0} into equation 3.48, we obtain

$$\left(\frac{1}{v_p\Delta t} \sin\left(\frac{\omega\Delta t}{2}\right) \right)^2 = \left(\frac{1}{\Delta x} \sin\left(\frac{\bar{k}_x\Delta x}{2}\right) \right)^2 + \left(\frac{1}{\Delta y} \sin\left(\frac{\bar{k}_y\Delta y}{2}\right) \right)^2 \tag{3.49}$$

where $v_p = \sqrt{\mu\epsilon}$ is the phase velocity.

Equation 3.49 is the general numerical dispersion relation for the TM_z mode. Assuming $\Delta x = \Delta y = \Delta$ and writing $\bar{k}_x = \check{k}\cos(\phi)$ and $\bar{k}_y = \check{k}\sin(\phi)$, this equation can be written as

$$\begin{aligned}
\left(\frac{\Delta}{v_p \Delta t}\right)^2 \sin^2\left(\frac{\omega \Delta t}{2}\right) &= \sin^2\left(\frac{\Delta \check{k} \cos(\phi)}{2}\right) + \sin^2\left(\frac{\Delta \check{k} \sin(\phi)}{2}\right) \\
= \sin\left(\frac{\omega \Delta t}{2}\right) &= \frac{v_p \Delta t}{\Delta} \sqrt{\sin^2\left(\frac{\check{k} \cos(\phi) \Delta}{2}\right) + \sin^2\left(\frac{\check{k} \sin(\phi) \Delta}{2}\right)} \\
\rightarrow \omega & \\
= \frac{2}{\Delta t} \sin^{-1}\left(\frac{v_p \Delta t}{\Delta} \sqrt{\sin^2\left(\frac{\check{k} \cos(\phi) \Delta}{2}\right) + \sin^2\left(\frac{\check{k} \sin(\phi) \Delta}{2}\right)}\right) &
\end{aligned} \tag{3.50}$$

Dividing both sides of equation 3.50 by \check{k} leads the following equation

$$\begin{aligned}
\frac{\omega}{\check{k}} &= \check{v}_p \\
= \frac{2}{\check{k} \Delta t} \sin^{-1}\left(\frac{v_p \Delta t}{\Delta} \sqrt{\sin^2\left(\frac{\check{k} \cos(\phi) \Delta}{2}\right) + \sin^2\left(\frac{\check{k} \sin(\phi) \Delta}{2}\right)}\right) &
\end{aligned} \tag{3.51}$$

where $v_p = 1/\sqrt{(\mu\epsilon)}$ is the speed of light, \check{v}_p is numerical phase velocity and ϕ is the propagation direction with respect to x axes. It is obvious that both Δ and Δt affects numerical dispersion and should be carefully selected. Setting $\phi = 45^\circ$ and selecting $\Delta t = \frac{\Delta}{\sqrt{2}}$ in equation 3.51 leads to

$$\check{v}_p = v_p \text{ or } \left(\frac{\omega}{\check{v}_p}\right)^2 = \check{k}_x^2 + \check{k}_y^2 \tag{3.52}$$

That is numerical wave propagates exactly with the speed of light. Therefore, we can recover the ideal dispersion relation by selecting appropriate values. The dependence of \check{v}_p on propagation angle ϕ is called grid anisotropy. We demonstrate how the numerical phase velocity changes with propagation angle ϕ in figure 3.5 for $\Delta t = \frac{\Delta}{2v_p}$ and in figure 3.6 for

$$\Delta t = \frac{\Delta}{\sqrt{2}v_p}.$$

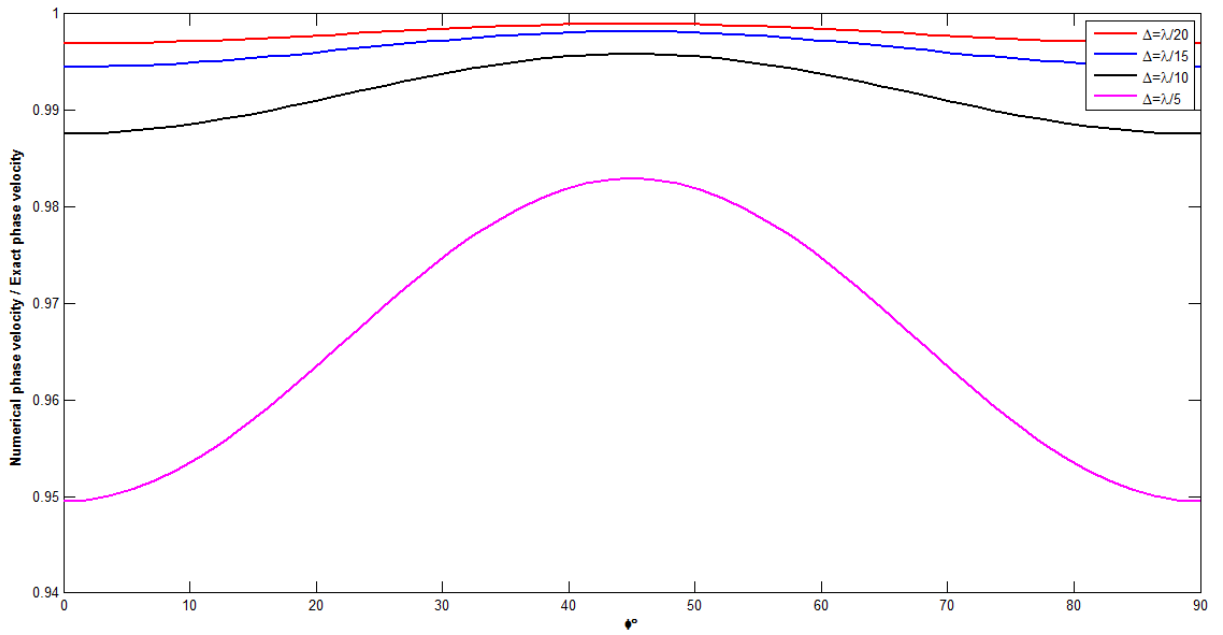


Figure 3.5 \bar{v}_p/v_p versus ϕ for $\Delta t = \Delta/2v_p$.

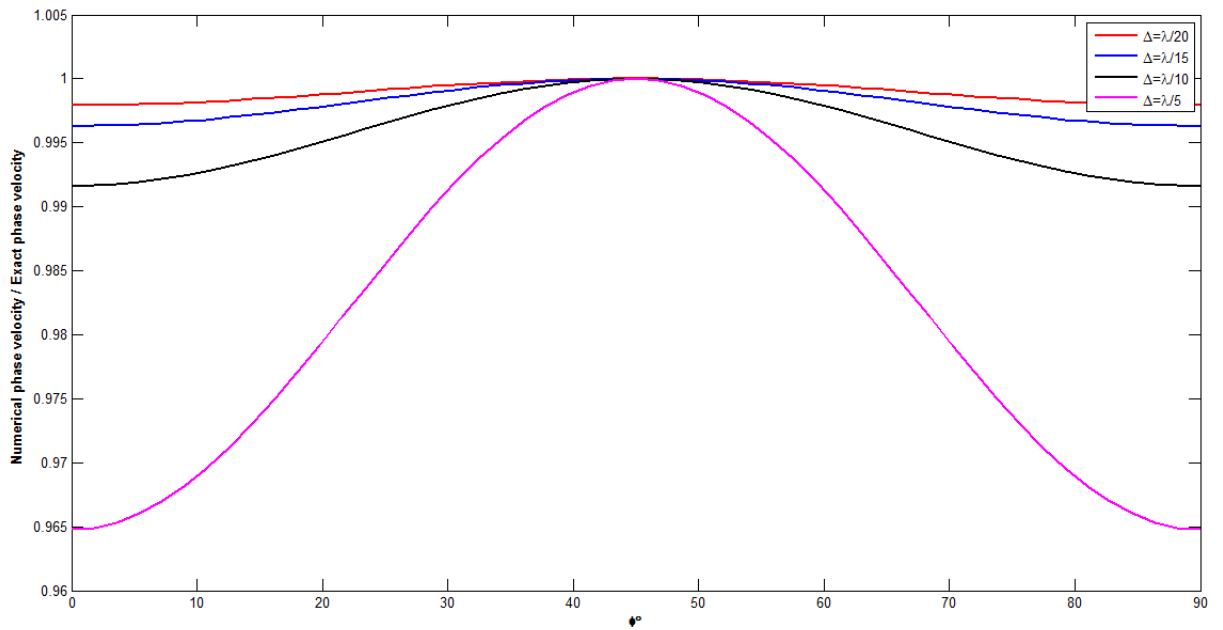


Figure 3.6 \bar{v}_p/v_p versus ϕ for $\Delta t = \Delta/\sqrt{2}v_p$.

It is evident that increasing sampling resolution decreases numerical dispersion error. What's more, we cannot totally eliminate numerical dispersion error because we are restricted to work with finite grid cells. For this reason, numerical dispersion error is inherited to FDTD algorithm, but this error is very small even for $\lambda/5$ resolution.

3.5 Stability

In this section, we analyze how selection of time step Δt affects stability of the FDTD algorithm. For this purpose, we will use complex-frequency analysis which allows for the possibility of a complex-valued numerical angular frequency, $\omega = \omega_{real} + j\omega_{imag}$ [23]. We start first by modifying the angular frequency term in equation 3.43 as follows

$$\begin{aligned} E_z|_{i,j}^n &= E_{z0} e^{j((\omega_{real} + j\omega_{imag})n\Delta t - \tilde{k}_x i \Delta x - \tilde{k}_y j \Delta y)} \\ &= E_z|_{i,j}^n = E_{z0} e^{(-\Delta t n \omega_{imag})} e^{j(\omega_{real} n \Delta t - \tilde{k}_x i \Delta x - \tilde{k}_y j \Delta y)} \end{aligned} \quad (3.53)$$

If the term ω_{imag} in equation 3.53 is positive, we have exponentially decreasing wave amplitude. On the other hand, if ω_{imag} is negative, we have exponentially increasing wave amplitude. In section 3.4 we have derived an expression of the numerical angular frequency ω which is written again for clarity

$$\omega = \frac{2}{\Delta t} \times \sin^{-1} \left(v_p \Delta t \sqrt{\frac{1}{\Delta x^2} \sin^2 \left(\frac{\tilde{k} \cos(\phi) \Delta x}{2} \right) + \frac{1}{\Delta y^2} \sin^2 \left(\frac{\tilde{k} \sin(\phi) \Delta y}{2} \right)} \right) \quad (3.54)$$

In this equation, if the term inside the arcsin function has value between 0 and 1, we obtain real numerical angular frequency. We can also observe from the equation 3.54 that the upper bound of the expression in square root is

$$\begin{aligned} &\sqrt{\frac{1}{\Delta x^2} \sin^2 \left(\frac{\tilde{k} \cos(\phi) \Delta x}{2} \right) + \frac{1}{\Delta y^2} \sin^2 \left(\frac{\tilde{k} \sin(\phi) \Delta y}{2} \right)} \\ &\leq \sqrt{\frac{1}{\Delta x^2} + \frac{1}{\Delta y^2}} \end{aligned} \quad (3.55)$$

Therefore, we can write

$$0 \leq v_p \Delta t \sqrt{\frac{1}{\Delta x^2} + \frac{1}{\Delta y^2}} \leq 1 \quad (3.56)$$

To ensure stability we should select the time step Δt as

$$\Delta t \leq \frac{1}{v_p \sqrt{\frac{1}{\Delta x^2} + \frac{1}{\Delta y^2}}} \quad (3.57)$$

When $\Delta x = \Delta y = \Delta$, equation 3.57 becomes

$$\Delta t \leq \frac{\Delta}{v_p \sqrt{2}} \quad (3.58)$$

This expression tells us that, the electromagnetic wave should travel at most one cell diagonally in one time step.

In a similar manner for 3D FDTD, the time step Δt should be selected as

$$\Delta t \leq \frac{1}{v_p \sqrt{\frac{1}{\Delta x^2} + \frac{1}{\Delta y^2} + \frac{1}{\Delta z^2}}} \quad (3.59)$$

3.6 Perfectly Matched Layer Boundary Conditions

Scattering and radiation problems require the simulation space which extends infinity. Due to the finite nature of computers we cannot use infinite number of cells. Even if we are interested in near fields, we need to enlarge total simulation space to prevent reflections from the boundaries. However, increasing total simulation space increases the computational burden excessively. So far, several methods proposed to overcome this difficulty [23]. These methods split into two groups, one called absorbing boundary conditions (ABC), the other called radiation boundary conditions (RBC). RBCs require the storage of field components more than one time step back depending on the order of accuracy. Hence, they can cause out of memory errors for large problems. Also since they are a function of incident angle, they can give spurious reflections for grazing angles. On the other hand, ABCs don't require the storage of field components more than one time step back, and give more accurate results with compare to RBCs. Among ABCs, the perfectly matched layer (PML) boundaries are very popular and easy to implement. PML is a finite-thickness special lossy medium which is placed at the terminals of the computational space to create perfectly matching condition for all angles and frequencies.

Because of being frequency and angle independent, they are used in scattering and radiation problems frequently. There are several types of PMLs found in literature such as uniaxial PML (UPML), convolutional PML (CPML), split-field PML (SPML), and the detailed comparison of their properties can be found in [24]. In this dissertation we preferred to use UPML so this type of PML will be explained. We will start by reviewing electromagnetic wave behavior at the boundary of two dissimilar media to explain the underlying theory of PMLs.

3.6.1 Plane Wave Incident on a Lossy Medium

Considering a TM_z polarized field shown in figure 3.7 where the incident electric field phasor is given by

$$\begin{aligned}
 \mathbf{E}_i &= \vec{\mathbf{z}}e^{-jk_i \cdot \mathbf{r}} \\
 &= \vec{\mathbf{z}}e^{-j(k_i \cos(\theta_i)x + k_i \sin(\theta_i)y)} \\
 &= \vec{\mathbf{z}}e^{-j(k_{ix}x + k_{iy}y)}
 \end{aligned} \tag{3.60}$$

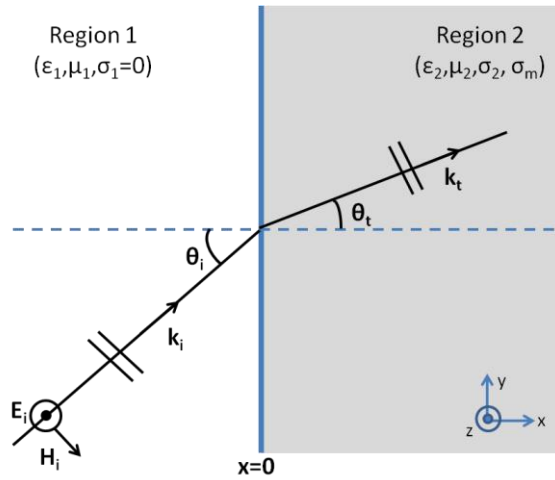


Figure 3.7 Plane wave incident on a lossy medium

The incident magnetic field is then calculated from

$$\begin{aligned}
\mathbf{H}_i &= -\frac{1}{j\omega u_1} \nabla \times \mathbf{E}_i = -\frac{1}{j\omega \mu_1} \begin{vmatrix} \vec{x} & \vec{y} & \vec{z} \\ \partial/\partial x & \partial/\partial y & \partial/\partial z \\ 0 & 0 & e^{-j(k_{ix}x+k_{iy}y)} \end{vmatrix} \\
&= -\frac{1}{j\omega \mu_1} (-jk_{iy}\vec{x} + jk_{ix}\vec{y}) e^{-j(k_{ix}x+k_{iy}y)} \\
&= \left[\vec{x} \frac{k_{iy}}{\omega u_1} - \vec{y} \frac{k_{ix}}{\omega \mu_1} \right] e^{-j(k_{ix}x+k_{iy}y)}
\end{aligned} \tag{3.61}$$

Assuming a presence of reflected wave and knowing that the angle of incidence equals to angle of reflection, we have

$$\mathbf{E}_r = \vec{z} \Gamma e^{-j(-k_{ix}x+k_{iy}y)} \tag{3.62}$$

where $\Gamma = \frac{|\mathbf{E}_r(0,y)|}{|\mathbf{E}_i(0,y)|}$ is the reflection coefficient. Notice that the change of sign in equation 3.62 due to the reflection. Then we can write the total electric fields in region 1 as

$$\mathbf{E}_{total} = \mathbf{E}_1 = \vec{z} (e^{-jk_{ix}x} + \Gamma e^{+jk_{ix}x}) e^{-jk_{iy}y} \tag{3.63}$$

In kind, using equation 3.61 we can write the total magnetic fields in region 1 as

$$\begin{aligned}
\mathbf{H}_{total} = \mathbf{H}_1 &= \vec{x} \frac{k_{iy}}{\omega \mu_1} (e^{-j(k_{ix}x)} + \Gamma e^{(k_{ix}x)}) e^{-j(k_{iy}y)} \\
&+ \vec{y} \frac{k_{ix}}{\omega \mu_1} (-e^{-j(k_{ix}x)} + \Gamma e^{(k_{ix}x)}) e^{-j(k_{iy}y)}
\end{aligned} \tag{3.64}$$

Now we can consider the electromagnetic fields in region 2 which is lossy medium characterized with the parameters σ_2 and σ_m . For this reason we can write the time harmonic Maxwell's equations for general lossy media as follows

$$\nabla \times \mathbf{E} = -j\omega \mu \mathbf{H} - \sigma_m \mathbf{H} = -j\omega \underbrace{\mu \left(1 + \frac{\sigma_m}{j\omega \mu} \right)}_{=\mu_{eff}} \mathbf{H} \tag{3.65}$$

$$\nabla \times \mathbf{H} = j\omega \epsilon \mathbf{E} + \sigma \mathbf{E} = j\omega \underbrace{\epsilon \left(1 + \frac{\sigma}{j\omega \epsilon} \right)}_{=\epsilon_{eff}} \mathbf{E} \tag{3.66}$$

Therefore the transmitted electric field in Region 2 can be written as

$$\mathbf{E}_t = \mathbf{E}_2 = \vec{\mathbf{z}}T e^{-j(k_{tx}x+k_{ty}y)} \quad (3.67)$$

where $T = \left| \frac{E_T(0,y)}{E_i(0,y)} \right|$ is the transmission coefficient. The magnetic fields in Region 2 are calculated using equation 3.65 as follows

$$\begin{aligned} \mathbf{H}_t &= -\frac{1}{j\omega u_2 \left(1 + \frac{\sigma_m}{j\omega\mu_2}\right)} \nabla \times \mathbf{E}_t \\ &= -j\omega u_2 \left(1 + \frac{\sigma_m}{j\omega\mu_2}\right) \begin{vmatrix} \vec{\mathbf{x}} & \vec{\mathbf{y}} & \vec{\mathbf{z}} \\ \frac{\partial}{\partial x} & \frac{\partial}{\partial y} & \frac{\partial}{\partial z} \\ 0 & 0 & T e^{-j(k_{tx}x+k_{ty}y)} \end{vmatrix} \\ &= \left[\vec{\mathbf{x}} \frac{k_{ty}}{\omega u_2 \left(1 + \frac{\sigma_m}{j\omega\mu_2}\right)} - \vec{\mathbf{y}} \frac{k_{tx}}{\omega u_2 \left(1 + \frac{\sigma_m}{j\omega\mu_2}\right)} \right] T e^{-j(k_{tx}x+k_{ty}y)} \end{aligned} \quad (3.68)$$

where

$$\begin{aligned} k_{tx} &= k_t \cos\theta, \quad k_{ty} = k_t \sin\theta \\ k_t^2 &= k_{tx}^2 + k_{ty}^2 = \omega^2 \mu_{eff} \epsilon_{eff} \end{aligned} \quad (3.69)$$

is the propagation constant.

Owing to the boundary condition that is the continuity of the tangential fields at the interface ($x=0$), the propagation in the y direction must be same in both media yields

$$\vec{\mathbf{z}}(1 + \Gamma) e^{-jk_{iy}y} = \vec{\mathbf{z}}T e^{-j(k_{ty}y)} \quad (3.70)$$

Thus we can say that

$$\begin{aligned} 1 + \Gamma &= T \\ k_{iy} &= k_{ty} = k_i \sin\theta \end{aligned} \quad (3.71)$$

Plugging equation 3.71 into 3.69 and solving for k_{tx} yields

$$k_{tx} = \sqrt{(\omega^2 \epsilon_2 \mu_2) \left(1 + \frac{\sigma_m}{j\omega \mu_2}\right) \left(1 + \frac{\sigma_m}{j\omega \epsilon_2}\right) - k_{ty}^2} \quad (3.72)$$

Equating y component of the magnetic fields at x=0 we obtain

$$\vec{y} \frac{k_{ix}}{\omega \mu_1} (-1 + \Gamma) e^{-j(k_{1y}y)} = -\vec{y} \frac{k_{tx}}{\omega u_2 \left(1 + \frac{\sigma_m}{j\omega \mu_2}\right)} T e^{-j(k_{ty}y)} \quad (3.73)$$

In this case, we can say that

$$-1 + \Gamma = -\frac{\mu_1 k_{tx}}{u_2 \left(1 + \frac{\sigma_m}{j\omega \mu_2}\right) k_{ix}} T \quad (3.74)$$

The reflection and transmission coefficients are given by [25]

$$\Gamma = \frac{\eta_2 \cos \theta_i - \eta_1 \cos \theta_t}{\eta_2 \cos \theta_i + \eta_1 \cos \theta_t} = \frac{\frac{k_{tx}}{\omega \epsilon_2 \left(1 + \frac{\sigma_2}{j\omega \epsilon_2}\right)} - \frac{k_{ix}}{\omega \epsilon_1}}{\frac{k_{tx}}{\omega \epsilon_2 \left(1 + \frac{\sigma_2}{j\omega \epsilon_2}\right)} + \frac{k_{ix}}{\omega \epsilon_1}} \quad (3.75)$$

and

$$T = 1 + \Gamma = \frac{\frac{2k_{tx}}{\omega \epsilon_2 \left(1 + \frac{\sigma_2}{j\omega \epsilon_2}\right)}}{\frac{k_{tx}}{\omega \epsilon_2 \left(1 + \frac{\sigma_2}{j\omega \epsilon_2}\right)} + \frac{k_{ix}}{\omega \epsilon_1}} \quad (3.76)$$

Reflection coefficient will be zero only if the terms in the numerator of equation 3.75 cancel. Also it is seen that, for an arbitrary incident angle $\theta_i \neq 0$ we have complex and non-zero reflection number. Assuming the incident wave $\theta_i = 0$, the expression in equation 3.75 reduces to

$$\Gamma = \frac{\eta_2 - \eta_1}{\eta_2 + \eta_1} \quad (3.77)$$

where

$$\eta_2 = \sqrt{\frac{\mu_{eff}}{\epsilon_{eff}}} = \sqrt{\frac{\left(\mu_2 \left(1 + \frac{\sigma_m}{j\omega\mu_2}\right)\right)}{\left(\epsilon_2 \left(1 + \frac{\sigma_2}{j\omega\epsilon_2}\right)\right)}} \quad (3.78)$$

and

$$\eta_1 = \sqrt{\frac{\mu_1}{\epsilon_1}}$$

Selecting $\mu_1 = \mu_2, \epsilon_1 = \epsilon_2$ and $\sigma_m = \frac{\sigma\mu_1}{\epsilon_1}$ yields that $\Gamma = 0$, perfectly matching wave transmission at the boundary. But, for oblique incidence, the numerator of the term in equation 3.75 cannot be zero and there will always be reflection from region 2.

3.6.2 Uniaxial Perfectly Matched Layer (PML)

Among the different versions of the PML, the uniaxial perfectly matched layer (PML) is arguably simplest to understand and has been broadly used in the FDTD simulations. In UPML, lossy layer is described as an artificial anisotropic uniaxial absorbing material which is composed of both electric and magnetic permittivity tensors. The main advantage of the UPML is that we don't require changing our code in both computational region and PML region. Therefore, the FDTD algorithm remains same in both domains. The placement of the PML in computational space is shown in figure 3.8.

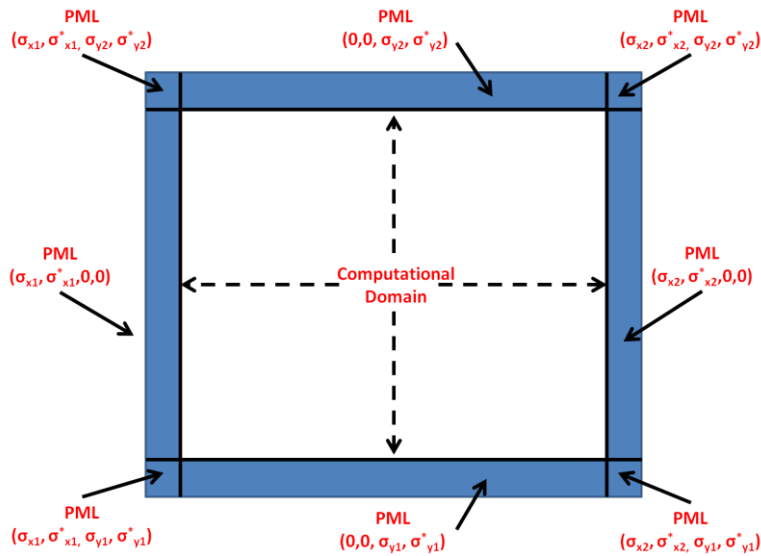


Figure 3.8 Placement of PML in computational domain

We can assume that the region 2 ($x > 0$) in figure 3.7, as an anisotropic uniaxial medium which is rotationally symmetric around the x axis and having the electrical permittivity and magnetic permeability tensors:

$$\overline{\overline{\epsilon}}_2 = \epsilon_2 \begin{bmatrix} a & 0 & 0 \\ 0 & b & 0 \\ 0 & 0 & b \end{bmatrix} \quad \overline{\overline{\mu}}_2 = \mu_2 \begin{bmatrix} c & 0 & 0 \\ 0 & d & 0 \\ 0 & 0 & d \end{bmatrix} \quad (3.79)$$

Also we assume that a TE polarized time-harmonic wave $\mathbf{H}_i = \mathbf{H}_0 e^{-j(k_{1x}x + k_{1y}y)}$ propagates through region 2. As we did in previous chapter for *TM* mode, we can write total electric and magnetic fields in the region 1 as

$$\mathbf{H}_1 = \vec{\mathbf{z}}\mathbf{H}_0(1 + \Gamma e^{j(2k_{1x}x)})e^{-j(k_{1x}x + k_{1y}y)} \quad (3.80)$$

$$\begin{aligned} \mathbf{E}_1 = \mathbf{H}_0 \left[-\vec{\mathbf{x}} \frac{k_{1y}}{\omega\epsilon_1} (1 + \Gamma e^{j(2k_{1x}x)}) \right. \\ \left. + \vec{\mathbf{y}} \frac{k_{1x}}{\omega\epsilon_1} (1 - \Gamma e^{j(2k_{1x}x)}) \right] e^{-j(k_{1x}x + k_{1y}y)} \end{aligned} \quad (3.81)$$

Electromagnetic waves in region 2 satisfy the Maxwell's equations in a general anisotropic medium which can be expressed in phasor form as:

$$\nabla_x \mathbf{E} = -j\omega \overline{\overline{\mu}}_2 \mathbf{H} \text{ or } \mathbf{k}_2 \mathbf{x} \mathbf{E} = \omega \overline{\overline{\mu}}_2 \mathbf{H} \quad (3.82)$$

$$\nabla_x \mathbf{H} = j\omega \overline{\overline{\epsilon}}_2 \mathbf{E} \text{ or } \mathbf{k}_2 \mathbf{x} \mathbf{H} = -\omega \overline{\overline{\epsilon}}_2 \mathbf{E} \quad (3.83)$$

where

$$\mathbf{k}_2 = \vec{\mathbf{x}}k_{2x} + \vec{\mathbf{y}}k_{2y} \quad (3.84)$$

is the wavevector in region 2. Combining equations 3.82 and 3.83 leads to wave equation given as:

$$\mathbf{k}_2 \mathbf{x} \left(\overline{\overline{\epsilon}}^{-1} \mathbf{k}_2 \right) \mathbf{x} \mathbf{H} + \omega^2 \overline{\overline{\mu}}_2 \mathbf{H} = 0 \quad (3.85)$$

which can also be written in matrix form as:

$$\begin{bmatrix} \omega^2 \mu_2 \epsilon_2 c - k_{2y}^2 b^{-1} & k_{2x} k_{2y} b^{-1} & 0 \\ k_{2x} k_{2y} b^{-1} & k_{2x}^2 d - k_{2x}^2 b^{-1} & 0 \\ 0 & 0 & \omega^2 \mu_2 \epsilon_2 d - k_{2x}^2 b^{-1} - k_{2y}^2 a^{-1} \end{bmatrix} \begin{bmatrix} H_x \\ H_y \\ H_z \end{bmatrix} = 0 \quad (3.8)$$

The solutions of the determinant of the matrix in equation 3.86 give the relationship between the wave numbers that is called dispersion relation as we mentioned in section 3.4. There are two solutions of equation 3.86 which are called TE mode ($H_x, H_y = 0$) and TM mode ($H_z = 0$). We assume only TE mode solution which is obtained at setting $H_x, H_y = 0$ in equation 3.86 as

$$\omega^2 \mu_2 \epsilon_2 d - k_{2x}^2 b^{-1} - k_{2y}^2 a^{-1} = 0 \quad (3.87)$$

The wave transmitted in region 2 can be expressed in a manner similar to equation 3.68 as

$$\begin{aligned} \mathbf{H}_2 &= \vec{\mathbf{z}} \mathbf{H}_0 T e^{-j(k_{2x}x + k_{2y}y)} \\ \mathbf{E}_2 &= \mathbf{H}_0 \left[-\vec{\mathbf{x}} \frac{k_{2y}}{\omega \epsilon_2 a} + \vec{\mathbf{y}} \frac{k_{2x}}{\omega \epsilon_2 b} \right] T e^{-j(k_{2x}x + k_{2y}y)} \end{aligned} \quad (3.88)$$

Owing to the boundary condition that is the continuity of the tangential fields at the interface ($x=0$), the propagation in the y direction must be same in both media yields

$$\begin{aligned} \mathbf{H}_1(\mathbf{0}, \mathbf{y}) &= \mathbf{H}_2(\mathbf{0}, \mathbf{y}) \\ \vec{\mathbf{z}} \mathbf{H}_0 (1 + \Gamma) e^{-j(k_{1y}y)} &= \vec{\mathbf{z}} \mathbf{H}_0 T e^{-j(k_{2y}y)} \\ \rightarrow 1 + \Gamma &= T \text{ and } k_{1y} = k_{2y} \end{aligned} \quad (3.89)$$

and

$$\begin{aligned} \mathbf{E}_1(\mathbf{0}, \mathbf{y}) &= \mathbf{E}_2(\mathbf{0}, \mathbf{y}) \\ \mathbf{H}_0 \left[\vec{\mathbf{y}} \frac{k_{1x}}{\omega \epsilon_1} (1 - \Gamma) \right] e^{-j(k_{1y}y)} &= \mathbf{H}_0 \left[\vec{\mathbf{y}} \frac{k_{2x}}{\omega \epsilon_2 b} \right] T e^{-j(k_{2y}y)} \\ \rightarrow \frac{k_{1x}}{\omega \epsilon_1} (1 - \Gamma) &= \frac{k_{2x}}{\omega \epsilon_2 b} T = \frac{k_{2x}}{\omega \epsilon_2 b} (1 + \Gamma) \end{aligned} \quad (3.90)$$

Since $k_{1y} = k_{2y}$ for all incident angles, we can put this equality into equation 3.87 to obtain the value of k_{2x} as

$$k_{2x} = \sqrt{\omega^2 \epsilon_2 \mu_2 b d - k_{1y}^2 a^{-1} b} \quad (3.91)$$

What's more, we can find the reflection coefficient from 3.90 as

$$\begin{aligned} \frac{k_{1x}}{\omega \epsilon_1} (1 - \Gamma) &= \frac{k_{2x}}{\omega \epsilon_2 b} (1 + \Gamma) \\ \Gamma &= \frac{k_{1x} \omega \epsilon_2 b - k_{2x} \omega \epsilon_1}{k_{1x} \omega \epsilon_2 b + k_{2x} \omega \epsilon_1} = \frac{k_{1x} \epsilon_2 - k_{2x} \epsilon_1 b^{-1}}{k_{1x} \epsilon_2 + k_{2x} \epsilon_1 b^{-1}} \end{aligned} \quad (3.92)$$

To achieve perfectly matching at the boundary, we need to have $\Gamma = 0$ which means that the nominator of equation 3.92 should be zero. From inspection, selecting $\epsilon_2 = \epsilon_1$, $\mu_1 = \mu_2$, $d = b$ and $a^{-1} = b$ yields

$$k_{2x} = \sqrt{\omega^2 \epsilon_1 \mu_1 b^2 - k_{1y}^2 b^2} = b \sqrt{k_1^2 - k_{1y}^2} = b k_{1x} \quad (3.93)$$

Putting equation 3.93 into equation 3.92 we have $\Gamma = 0$ for all incidence angles and k_{1x} . Thus the incident wave penetrates into region 2 without any reflection. Since we have found k_{2x} in equation 3.93, we can put this into equation 3.88 to analyze the wave behavior in region 2 as

$$\begin{aligned} \mathbf{H}_2 &= \underbrace{\vec{\mathbf{z}} \mathbf{H}_0}_{=1} \mathbb{T} e^{-j(b k_{1x} x + k_{1y} y)} \\ &\quad \text{since } \Gamma=0 \\ \mathbf{E}_2 &= \mathbf{H}_0 \left[-\vec{\mathbf{x}} \frac{k_{1y}}{\omega \epsilon_2 a} + \vec{\mathbf{y}} \frac{k_{1x}}{\omega \epsilon_2} \right] e^{-j(b k_{1x} x + k_{1y} y)} \end{aligned} \quad (3.94)$$

Selecting $b = 1 - \frac{\sigma_x}{j \omega \epsilon_1}$ yields

$$\mathbf{H}_2 = \vec{\mathbf{z}} \mathbf{H}_0 e^{-j(k_{1x} x + k_{1y} y)} e^{-\frac{\sigma_x x k_1}{\omega \epsilon}} \quad (3.95)$$

It is obvious that the magnetic field attenuates exponentially through the propagation in region 2 for all incident wave angles and k_{1x} . In a similar manner the electric field also undergoes an exponential decay through the propagation in region 2. The same analysis can be performed for TM mode. But in this case we need to replace b with d and a with c

and set $c^{-1} = d$ for reflectionless propagation. In sum, we can write the permittivity and permeability tensors to have $\Gamma = 0$ at the boundary $x = 0$ as

$$\overline{\overline{\epsilon}}_2 = \epsilon_1 \overline{\overline{s}}; \overline{\overline{\mu}}_2 = \mu_2 \overline{\overline{s}}; \overline{\overline{s}} = \begin{bmatrix} s_x^{-1} & 0 & 0 \\ 0 & s_x & 0 \\ 0 & 0 & s_x \end{bmatrix} \quad (3.96)$$

UPML extension for 3D case can be obtained easily by considering 3D case is a composition of individual lossy layers. That is, we need to place individual lossy layers at the front ends of the x, y and z dimensions of computational space. Then, the electric permittivity and magnetic permeability tensors will be in the form as

$$\overline{\overline{s}} = \begin{bmatrix} s_x^{-1} & 0 & 0 \\ 0 & s_x & 0 \\ 0 & 0 & s_x \end{bmatrix} \begin{bmatrix} s_y^{-1} & 0 & 0 \\ 0 & s_y & 0 \\ 0 & 0 & s_y \end{bmatrix} \begin{bmatrix} s_z^{-1} & 0 & 0 \\ 0 & s_z & 0 \\ 0 & 0 & s_z \end{bmatrix} \quad (3.97)$$

$$\overline{\overline{s}} = \begin{bmatrix} s_x^{-1} s_y s_z & 0 & 0 \\ 0 & s_x s_y^{-1} s_z & 0 \\ 0 & 0 & s_x s_y s_z^{-1} \end{bmatrix}$$

where

$$s_x = K_x + \frac{\sigma_x}{j\omega\epsilon_1}, s_y = K_y + \frac{\sigma_y}{j\omega\epsilon_1} \text{ and } s_z = K_z + \frac{\sigma_z}{j\omega\epsilon_1} \quad (3.98)$$

Here the parameters K_x, K_y and K_z are introduced for allowing non-unity real part. To use this tensor in FDTD algorithm we need to set non-zero conductivity at appropriate boundaries as demonstrated in figure 3.8. For example at $y = 0$ and $y = y_{total}$ we need to set $\sigma_x = \sigma_z = 0$.

3.6.3 UPML Algorithm

In this section, we will derive 3D numerical algorithm for implementing uniaxial perfectly matched layer medium formulated previously. Maxwell's equations for general anisotropic media are given in phasor form by equations 3.82 and 3.83, repeated below for convenience:

$$\nabla \times \mathbf{E} = -j\omega \overline{\overline{\mu}}_2 \mathbf{H} \text{ or } \mathbf{k}_2 \times \mathbf{E} = \omega \overline{\overline{\mu}}_2 \mathbf{H} \quad (3.99)$$

$$\nabla \times \mathbf{H} = j\omega \overline{\epsilon_2} \mathbf{E} \text{ or } \mathbf{k}_2 \times \mathbf{H} = -\omega \overline{\epsilon_2} \mathbf{E} \quad (3.100)$$

Writing the curl operator of equation 3.100 in matrix form and using the tensor which is introduced in equation 3.97 leads to

$$\begin{bmatrix} \frac{\partial H_z}{\partial y} - \frac{\partial H_y}{\partial z} \\ \frac{\partial H_x}{\partial z} - \frac{\partial H_z}{\partial x} \\ \frac{\partial H_y}{\partial x} - \frac{\partial H_x}{\partial y} \end{bmatrix} = j\omega\epsilon \begin{bmatrix} s_x^{-1}s_y s_z & 0 & 0 \\ 0 & s_x s_y^{-1} s_z & 0 \\ 0 & 0 & s_x s_y s_z^{-1} \end{bmatrix} = \begin{bmatrix} E_x \\ E_y \\ E_z \end{bmatrix} \quad (3.101)$$

Then we have from the first row of the matrix equation:

$$\frac{\partial H_z}{\partial y} - \frac{\partial H_y}{\partial z} = j\omega\epsilon \left[\frac{\left(K_y + \frac{\sigma_y}{j\omega\epsilon}\right) \left(K_z + \frac{\sigma_z}{j\omega\epsilon}\right)}{\left(K_x + \frac{\sigma_x}{j\omega\epsilon}\right)} \right] E_x \quad (3.102)$$

At this point, it is instructive to give some properties of the phasor to time domain transformations.

$$\frac{d}{dt} g(t) \leftrightarrow j\omega \tilde{G} \quad (3.103)$$

$$\int g(t) \leftrightarrow \frac{1}{j\omega} \tilde{G} \quad (3.104)$$

Converting equation 3.102 directly from phasor domain to time domain requires integration because of the term $j\omega\epsilon + \sigma_x$ in the denominator and integration is very computationally expensive process especially for large problems. To overcome this difficulty, we can use interim variable \mathbf{D} which is not physical and formed as

$$\begin{aligned} D_x &= \epsilon \frac{s_z}{s_x} E_x \\ D_y &= \epsilon \frac{s_x}{s_y} E_y \\ D_z &= \epsilon \frac{s_y}{s_z} E_z \end{aligned} \quad (3.105)$$

Then equation 3.101 becomes

$$\begin{bmatrix} \frac{\partial H_z}{\partial y} - \frac{\partial H_y}{\partial z} \\ \frac{\partial H_x}{\partial z} - \frac{\partial H_z}{\partial x} \\ \frac{\partial H_y}{\partial x} - \frac{\partial H_x}{\partial y} \end{bmatrix} = j\omega \begin{bmatrix} s_y & 0 & 0 \\ 0 & s_z & 0 \\ 0 & 0 & s_x \end{bmatrix} = \begin{bmatrix} D_x \\ D_y \\ D_z \end{bmatrix} \quad (3.106)$$

This leaves us to three equations which can be transformed into time domain easily by using equation 3.103. Moreover, since FDTD algorithm is based on discretizing partial derivatives in Maxwell's equations via centered difference approximation, we can apply the same approximation to discretize the resulting interim fields. This provides us to conserve our codes in both computational region and PML region with the expense of doubling field components which is explained soon. But anyway, this is computationally less expensive than calculating integrals. Considering the first equation in 3.106, we have

$$\frac{\partial H_z}{\partial y} - \frac{\partial H_y}{\partial z} = j\omega \left(\underbrace{K_y + \frac{\sigma_y}{j\omega\epsilon}}_{=s_y} \right) D_x = K_y j\omega D_x + \frac{\sigma_y}{\epsilon} D_x \quad (3.107)$$

Applying equation 3.103 to 3.107 yields

$$\frac{\partial H_z}{\partial y} - \frac{\partial H_y}{\partial z} = K_y \frac{\partial D_x}{\partial t} + \frac{\sigma_y}{\epsilon} D_x \quad (3.108)$$

The components of auxiliary fields D is assumed to be same location as the components of electric fields as shown in figure 3.1, therefore applying centered difference approximation to equation 3.108 gives

$$\begin{aligned} D_x|_{i+\frac{1}{2},j,k}^{n+1} &= \left(\frac{2\epsilon K_y - \sigma_y \Delta t}{2\epsilon K_y + \sigma_y \Delta t} \right) D_x|_{i+\frac{1}{2},j,k}^n \\ &+ \frac{2\epsilon \Delta t}{2\epsilon K_y + \sigma_y \Delta t} \left[\frac{H_z|_{i+\frac{1}{2},j+\frac{1}{2},k}^{n+\frac{1}{2}} - H_z|_{i+\frac{1}{2},j-\frac{1}{2},k}^{n+\frac{1}{2}}}{\Delta y} \right. \\ &\quad \left. - \frac{H_y|_{i+\frac{1}{2},j,k+\frac{1}{2}}^{n+\frac{1}{2}} - H_y|_{i+\frac{1}{2},j,k-\frac{1}{2}}^{n+\frac{1}{2}}}{\Delta z} \right] \end{aligned} \quad (3.109)$$

The other auxiliary field components can be derived in a similar manner, they are given here for the sake of completeness

$$D_y|_{i,j+\frac{1}{2},k}^{n+1} = \left(\frac{2\epsilon K_z - \sigma_z \Delta t}{2\epsilon K_z + \sigma_z \Delta t} \right) D_y|_{i,j+\frac{1}{2},k}^n$$

$$+ \frac{2\epsilon \Delta t}{2\epsilon K_z + \sigma_z \Delta t} \left[\frac{H_x|_{i,j+\frac{1}{2},k+\frac{1}{2}}^{n+\frac{1}{2}} - H_x|_{i,j+\frac{1}{2},k-\frac{1}{2}}^{n+\frac{1}{2}}}{\Delta z} - \frac{H_z|_{i+\frac{1}{2},j+\frac{1}{2},k}^{n+\frac{1}{2}} - H_z|_{i-\frac{1}{2},j+\frac{1}{2},k}^{n+\frac{1}{2}}}{\Delta x} \right] \quad (3.110)$$

$$D_z|_{i,j,k+\frac{1}{2}}^{n+1} = \left(\frac{2\epsilon K_x - \sigma_x \Delta t}{2\epsilon K_x + \sigma_x \Delta t} \right) D_z|_{i,j,k+\frac{1}{2}}^n$$

$$+ \frac{2\epsilon \Delta t}{2\epsilon K_x + \sigma_x \Delta t} \left[\frac{H_y|_{i+\frac{1}{2},j,k+\frac{1}{2}}^{n+\frac{1}{2}} - H_y|_{i-\frac{1}{2},j,k+\frac{1}{2}}^{n+\frac{1}{2}}}{\Delta x} - \frac{H_x|_{i,j+\frac{1}{2},k+\frac{1}{2}}^{n+\frac{1}{2}} - H_x|_{i,j-\frac{1}{2},k+\frac{1}{2}}^{n+\frac{1}{2}}}{\Delta y} \right] \quad (3.111)$$

Now we need to convert interim fields back to electric field components. This is also can be accomplished easily as shown for the x component:

$$D_x = \epsilon \frac{S_z}{S_x} E_x \rightarrow s_x D_x = \epsilon s_z E_x$$

$$\left(K_x + \frac{\sigma_x}{j\omega\epsilon} \right) D_x = \epsilon \left(K_z + \frac{\sigma_z}{j\omega\epsilon} \right) E_x \quad (3.112)$$

$$j\omega K_x D_x + \frac{\sigma_x}{\epsilon} D_x = j\omega\epsilon K_z E_x + \sigma_z E_x$$

Applying equation 3.103 to equation 3.112 leads

$$K_x \frac{\partial D_x}{\partial t} + \frac{\sigma_x}{\epsilon} D_x = \epsilon K_z \frac{\partial E_x}{\partial t} + \sigma_z E_x \quad (3.113)$$

Discretization of equation 3.113 yields update equation for the x component of the electric field:

$$\begin{aligned}
E_x|_{i+\frac{1}{2},j,k}^{n+1} &= \left(\frac{2\epsilon K_z - \sigma_z \Delta t}{2\epsilon K_z + \sigma_z \Delta t} \right) E_x|_{i+\frac{1}{2},j,k}^n \\
&+ \frac{1}{\epsilon} \left(\frac{2\epsilon K_x + \sigma_x \Delta t}{2\epsilon K_z + \sigma_z \Delta t} \right) D_x|_{i+\frac{1}{2},j,k}^{n+1} - \frac{1}{\epsilon} \left(\frac{2\epsilon K_x - \sigma_x \Delta t}{2\epsilon K_z + \sigma_z \Delta t} \right) D_x|_{i+\frac{1}{2},j,k}^n
\end{aligned} \tag{3.114}$$

The same analysis can be repeated for the remaining components of electric fields, and given as follows

$$\begin{aligned}
E_y|_{i,j+\frac{1}{2},k}^{n+1} &= \left(\frac{2\epsilon K_x - \sigma_x \Delta t}{2\epsilon K_x + \sigma_x \Delta t} \right) E_y|_{i,j+\frac{1}{2},k}^n \\
&+ \frac{1}{\epsilon} \left(\frac{2\epsilon K_y + \sigma_y \Delta t}{2\epsilon K_x + \sigma_x \Delta t} \right) D_y|_{i,j+\frac{1}{2},k}^{n+1} - \frac{1}{\epsilon} \left(\frac{2\epsilon K_y - \sigma_y \Delta t}{2\epsilon K_x + \sigma_x \Delta t} \right) D_y|_{i,j+\frac{1}{2},k}^n
\end{aligned} \tag{3.115}$$

$$\begin{aligned}
E_z|_{i,j,k+\frac{1}{2}}^{n+1} &= \left(\frac{2\epsilon K_y - \sigma_y \Delta t}{2\epsilon K_y + \sigma_y \Delta t} \right) E_z|_{i,j,k+\frac{1}{2}}^n \\
&+ \frac{1}{\epsilon} \left(\frac{2\epsilon K_z + \sigma_z \Delta t}{2\epsilon K_y + \sigma_y \Delta t} \right) D_z|_{i,j,k+\frac{1}{2}}^{n+1} - \frac{1}{\epsilon} \left(\frac{2\epsilon K_z - \sigma_z \Delta t}{2\epsilon K_y + \sigma_y \Delta t} \right) D_z|_{i,j,k+\frac{1}{2}}^n
\end{aligned} \tag{3.116}$$

Thus far, we are concerned with the electric field components. The magnetic fields can be calculated in a similar manner by writing the curl operator of equation 3.99 in matrix form as follows

$$\begin{aligned}
\begin{bmatrix} \frac{\partial E_z}{\partial y} - \frac{\partial E_y}{\partial z} \\ \frac{\partial E_x}{\partial z} - \frac{\partial E_z}{\partial x} \\ \frac{\partial E_y}{\partial x} - \frac{\partial E_x}{\partial y} \end{bmatrix} &= -j\omega\mu \begin{bmatrix} s_x^{-1}s_y s_z & 0 & 0 \\ 0 & s_x s_y^{-1}s_z & 0 \\ 0 & 0 & s_x s_y s_z^{-1} \end{bmatrix} \\
&= \begin{bmatrix} H_x \\ H_y \\ H_z \end{bmatrix}
\end{aligned} \tag{3.117}$$

In the same way for electric fields, we introduce auxiliary field B to get rid of integrals as shown below:

$$B_x = \mu \frac{s_z}{s_x} H_x \quad B_y = \epsilon \frac{s_x}{s_y} H_y \quad B_z = \epsilon \frac{s_y}{s_z} H_z \tag{3.118}$$

Using equation 3.118 in equation 3.117 leads to

$$\begin{bmatrix} \frac{\partial E_z}{\partial y} - \frac{\partial E_y}{\partial z} \\ \frac{\partial E_x}{\partial z} - \frac{\partial E_z}{\partial x} \\ \frac{\partial E_y}{\partial x} - \frac{\partial E_x}{\partial y} \end{bmatrix} = -j\omega \begin{bmatrix} s_y & 0 & 0 \\ 0 & s_z & 0 \\ 0 & 0 & s_x \end{bmatrix} = \begin{bmatrix} B_x \\ B_y \\ B_z \end{bmatrix} \quad (3.119)$$

Considering the first equation in 3.119, we obtain the following equation

$$\begin{aligned} \frac{\partial E_z}{\partial y} - \frac{\partial E_y}{\partial z} &= -j\omega \left(K_y + \frac{\sigma_y}{j\omega\epsilon} \right) B_x = -j\omega K_y B_x - \frac{\sigma_y}{\epsilon} B_x \\ \rightarrow \frac{\partial E_z}{\partial y} - \frac{\partial E_y}{\partial z} &= -K_y \frac{\partial B_x}{\partial t} - \frac{\sigma_y}{\epsilon} B_x \end{aligned} \quad (3.120)$$

Applying centered difference approximation to the partial derivatives of equation 3.120 yields updating equation for the interim field component B_x whose spatial location is the same as H_x and shown in the figure 3.1.

$$\begin{aligned} B_x \Big|_{i,j+\frac{1}{2},k+\frac{1}{2}}^{n+\frac{1}{2}} &= \left(\frac{2\epsilon K_y - \sigma_y \Delta t}{2\epsilon K_y + \sigma_y \Delta t} \right) B_x \Big|_{i,j+\frac{1}{2},k+\frac{1}{2}}^{n-\frac{1}{2}} \\ + \left(\frac{2\epsilon \Delta t}{2\epsilon K_y + \sigma_y \Delta t} \right) &\left[\frac{E_y \Big|_{i,j+\frac{1}{2},k+1}^n - E_y \Big|_{i,j+\frac{1}{2},k}^n}{\Delta z} - \frac{E_z \Big|_{i,j+1,k+\frac{1}{2}}^n - E_z \Big|_{i,j,k+\frac{1}{2}}^n}{\Delta y} \right] \end{aligned} \quad (3.121)$$

Doing same analysis as in equation 3.120 for remaining interim fields we obtain

$$\begin{aligned} B_y \Big|_{i+\frac{1}{2},j,k+\frac{1}{2}}^{n+\frac{1}{2}} &= \left(\frac{2\epsilon K_z - \sigma_z \Delta t}{2\epsilon K_z + \sigma_z \Delta t} \right) B_y \Big|_{i+\frac{1}{2},j,k+\frac{1}{2}}^{n-\frac{1}{2}} \\ + \left(\frac{2\epsilon \Delta t}{2\epsilon K_z + \sigma_z \Delta t} \right) &\left[\frac{E_z \Big|_{i+1,j,k+\frac{1}{2}}^n - E_z \Big|_{i,j,k+\frac{1}{2}}^n}{\Delta x} - \frac{E_x \Big|_{i+\frac{1}{2},j,k+1}^n - E_x \Big|_{i+\frac{1}{2},j,k}^n}{\Delta z} \right] \end{aligned} \quad (3.122)$$

$$\begin{aligned} B_z \Big|_{i+\frac{1}{2},j+\frac{1}{2},k}^{n+\frac{1}{2}} &= \left(\frac{2\epsilon K_x - \sigma_x \Delta t}{2\epsilon K_x + \sigma_x \Delta t} \right) B_z \Big|_{i+\frac{1}{2},j+\frac{1}{2},k}^{n-\frac{1}{2}} \\ + \left(\frac{2\epsilon \Delta t}{2\epsilon K_x + \sigma_x \Delta t} \right) &\left[\frac{E_x \Big|_{i+\frac{1}{2},j+1,k}^n - E_x \Big|_{i+\frac{1}{2},j,k}^n}{\Delta y} - \frac{E_y \Big|_{i+1,j+\frac{1}{2},k}^n - E_y \Big|_{i,j+\frac{1}{2},k}^n}{\Delta x} \right] \end{aligned} \quad (3.123)$$

The relationship between the interim fields B and magnetic fields H is similar to that of interim field D and E and can be given as

$$\begin{aligned}
B_x &= \mu \frac{S_z}{S_x} H_x \text{ or } s_x B_x = \mu s_z H_x \\
\rightarrow \left(K_x + \frac{\sigma_x}{j\omega\epsilon} \right) B_x &= \mu \left(K_z + \frac{\sigma_z}{j\omega\epsilon} \right) H_x \\
\rightarrow j\omega K_x B_x + \frac{\sigma_x}{\epsilon} B_x &= j\omega\mu K_z H_x + \frac{\sigma_z}{\epsilon} \mu H_x
\end{aligned} \tag{3.124}$$

Applying inverse transformation to equation 3.124 yields

$$K_x \frac{\partial B_x}{\partial t} + \frac{\sigma_x}{\epsilon} B_x = K_z \mu \frac{\partial H_x}{\partial t} + \frac{\sigma_z}{\epsilon} H_x \tag{3.125}$$

Equation 3.125 can be discretized as

$$\begin{aligned}
H_x \Big|_{i,j+\frac{1}{2},k+\frac{1}{2}}^{n+\frac{1}{2}} &= \left(\frac{2\epsilon K_z - \sigma_z \Delta t}{2\epsilon K_z + \sigma_z \Delta t} \right) H_x \Big|_{i,j+\frac{1}{2},k+\frac{1}{2}}^{n-\frac{1}{2}} \\
+ \frac{1}{\mu} \left(\frac{2\epsilon K_x + \sigma_x \Delta t}{2\epsilon K_z + \sigma_z \Delta t} \right) B_x \Big|_{i,j+\frac{1}{2},k+\frac{1}{2}}^{n+\frac{1}{2}} & \\
- \frac{1}{\mu} \left(\frac{2\epsilon K_x - \sigma_x \Delta t}{2\epsilon K_z + \sigma_z \Delta t} \right) B_x \Big|_{i,j+\frac{1}{2},k+\frac{1}{2}}^{n-\frac{1}{2}} &
\end{aligned} \tag{3.126}$$

The remaining magnetic field components can be obtained in a similar manner as follows

$$\begin{aligned}
H_y \Big|_{i+\frac{1}{2},j,k+\frac{1}{2}}^{n+\frac{1}{2}} &= \left(\frac{2\epsilon K_x - \sigma_x \Delta t}{2\epsilon K_x + \sigma_x \Delta t} \right) H_y \Big|_{i+\frac{1}{2},j,k+\frac{1}{2}}^{n-\frac{1}{2}} \\
+ \frac{1}{\mu} \left(\frac{2\epsilon K_y + \sigma_y \Delta t}{2\epsilon K_x + \sigma_x \Delta t} \right) B_y \Big|_{i+\frac{1}{2},j,k+\frac{1}{2}}^{n+\frac{1}{2}} & \\
- \frac{1}{\mu} \left(\frac{2\epsilon K_y - \sigma_y \Delta t}{2\epsilon K_x + \sigma_x \Delta t} \right) B_y \Big|_{i+\frac{1}{2},j,k+\frac{1}{2}}^{n-\frac{1}{2}} &
\end{aligned} \tag{3.127}$$

$$\begin{aligned}
H_z|_{i+\frac{1}{2},j+\frac{1}{2},k}^{n+\frac{1}{2}} &= \left(\frac{2\epsilon K_y - \sigma_y \Delta t}{2\epsilon K_y + \sigma_y \Delta t} \right) H_z|_{i+\frac{1}{2},j+\frac{1}{2},k}^{n-\frac{1}{2}} \\
&+ \frac{1}{\mu} \left(\frac{2\epsilon K_z + \sigma_z \Delta t}{2\epsilon K_y + \sigma_y \Delta t} \right) B_z|_{i+\frac{1}{2},j+\frac{1}{2},k}^{n+\frac{1}{2}} \\
&\quad - \frac{1}{\mu} \left(\frac{2\epsilon K_z - \sigma_z \Delta t}{2\epsilon K_y + \sigma_y \Delta t} \right) B_y|_{i+\frac{1}{2},j+\frac{1}{2},k}^{n-\frac{1}{2}}
\end{aligned} \tag{3.128}$$

The implementation of the UPML algorithm requires two step for updating individual electric and magnetic fields. That is, we first need to solve interim fields and then calculate electric and magnetic fields from the interim fields as shown in the related equations. Also we need to store one time step previous values of the interim fields because the magnetic and electric field updates require the values of interim fields at time n or $n - \frac{1}{2}$. Although, we explain the algorithm of 3D UPML, reduction to 2D case is straightforward and explained briefly in section 3.3. We have taken three snapshots at different time steps to demonstrate the PML boundary condition in 2D TM_z mode as shown in figures 3.9, 3.10 and 3.11. We have injected Gaussian source at the center of the simulation space.

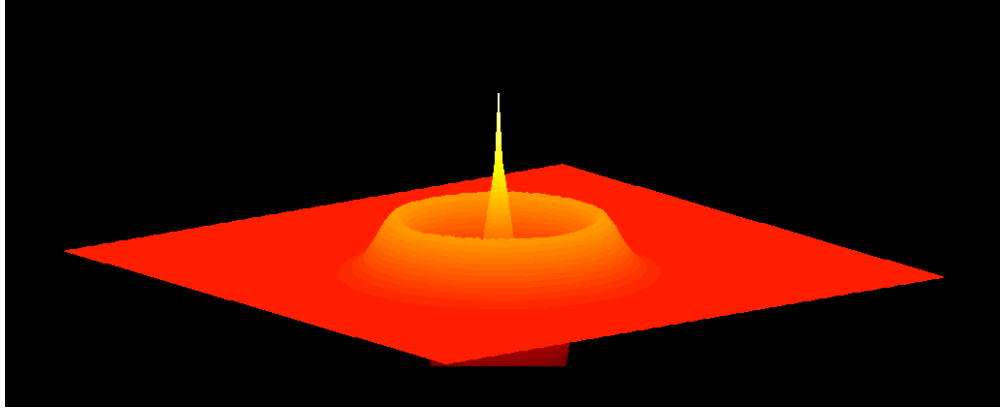


Figure 3.9 TM_z FDTD simulation snapshot at $t = 20\Delta t$

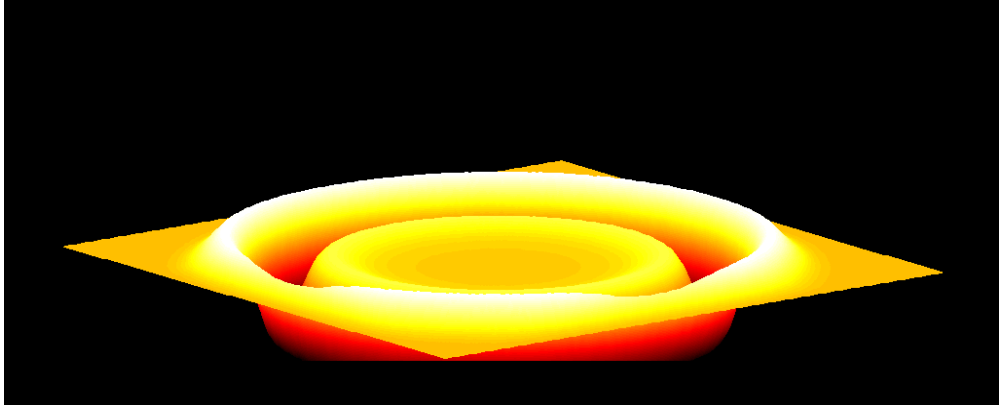


Figure 3.10 TM_z FDTD simulation snapshot at $t = 150\Delta t$

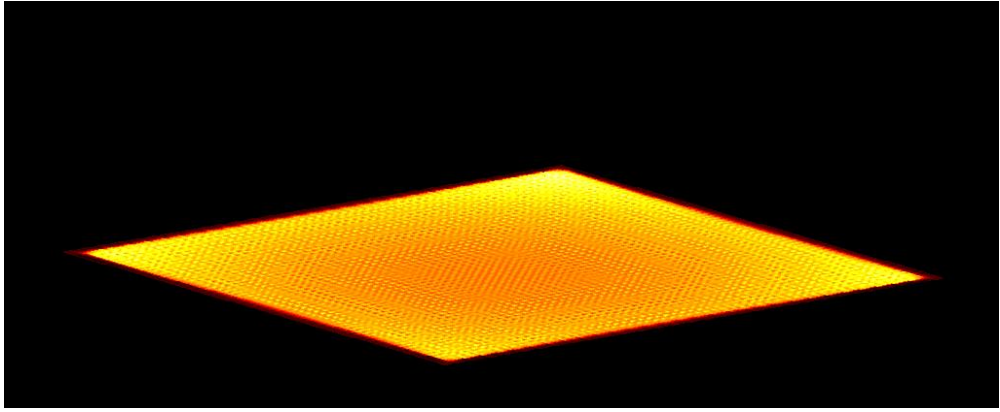


Figure 3.11 TM_z FDTD simulation snapshot at $t = 300\Delta t$

Source codes for this simulation can be found in Appendix 1. An ideal PML is reflectionless, if the parameters of the PML are selected properly as described previously. However, because of the numerical approximations, the PML in FDTD simulations cannot absorb the power penetrating into PML regions properly and consequently can lead to significant spurious reflections. To overcome this problem, we need to use multilayer PML instead [26]. The term multilayer means that the conductivity profile of the lossy layer changes with spatial increment. There are several methods to create such a multilayer PML but arguably most effective one is polynomial grading whose formulation is given as

$$\sigma_x(x) = \sigma_{x_{max}} \left(\frac{d-x}{d} \right)^m \quad (3.129)$$

where the parameter m is generally taken as 3 or 4. Also in equation 3.129, d is the thickness of the PML and σ_{max} is the maximum value of the conductivity which is expressed as:

$$\sigma_{x_{max}} = \frac{m + 1}{200\pi\sqrt{\epsilon_r}\Delta x} \quad (3.130)$$

Remaining conductivity profiles can be graded in similar manner by using equation 3.129.

3.7 Modeling PEC Objects

Modeling objects in FDTD plays important role for the accuracy of the simulation results. Standard FDTD algorithm explained so far uses staircase approximation to model objects in simulation space. In this approximation, if the center of cubic cell is embedded inside the perfectly electric conductance (PEC) object, all surrounding electric fields of this cell are set to zero. For 2D simulations, we can examine staircase approximation for TM_z mode and TE_z mode separately as follows: when modeling a PEC in TM_z mode, if an E_z node falls within the PEC, it is zero. In a TE_z mode, if an H_z node falls within the PEC, all surrounding electric fields are set to zero. All the magnetic fields are updated in the usual way for both 3D and 2D cases. Although this approach is very simple to use, it can lead significant errors for slanted or curved objects as shown in figure 3.12 for TE_z mode. In this figure, critical cells which constitute the boundary of pec object are marked with “x”. As it is seen, staircase approximation models missile radome very poorly and sharp corners resulted from the staircase approximation can lead to non-realistic diffracted fields. The level of staircase error can be reduced by increasing resolution but this increases computational burden significantly. To overcome this difficulty, several methods are proposed in the past decade. One solution of this problem is to use non-uniform meshing whose dimensions are smaller in specific regions to fit object boundaries. However, this approach suffers from the fact that it increases total number of cells and as a result computational burden. The second and more robust solution called contour-path modeling is based on deforming unit cells in specific regions to conform boundaries of PEC object. The drawback of this approach is that, we require complex meshing algorithm. Also, the reduction of the time step is necessary to avoid stability errors as will be explained soon.

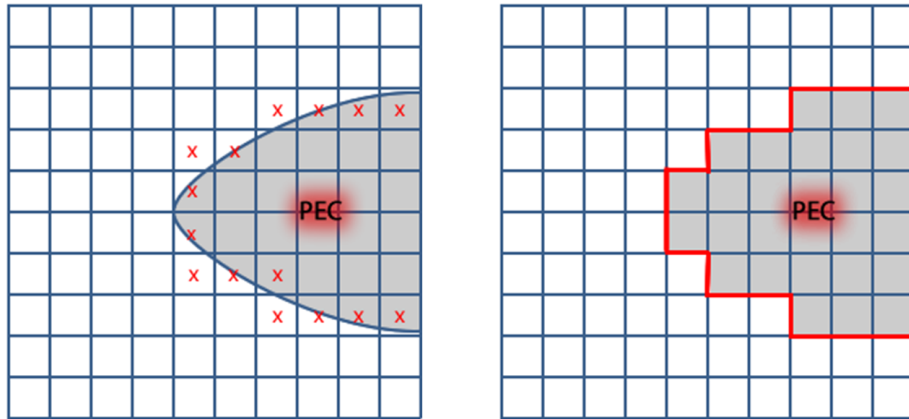


Figure 3.12 Staircase modeling missile radome

3.7.1 Day-Mitra Conformal FDTD

In 1997, Day-Mitra introduced conformal modeling techniques for PEC and dielectric structures which do not conform to Yee grid [26]. In this technique, only a modification of Faraday loop is required as shown in figure 3.13.

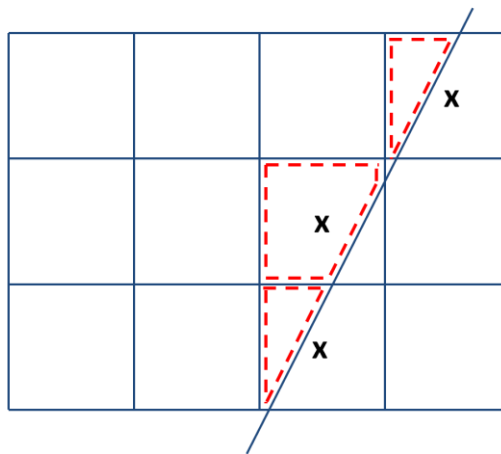


Figure 3.13 Modified Faraday loop in Day-Mitra technique

In this method, a conformal updating algorithm applied to individual partially filled cells, and the time step size needs to be reduced in accordance with the size and shape of the deformed cell. It is instructive to investigate deformed cells in the figure 3.13 separately. For this purpose three different scenarios for Day-Mitra conformal technique are presented in figure 3.14

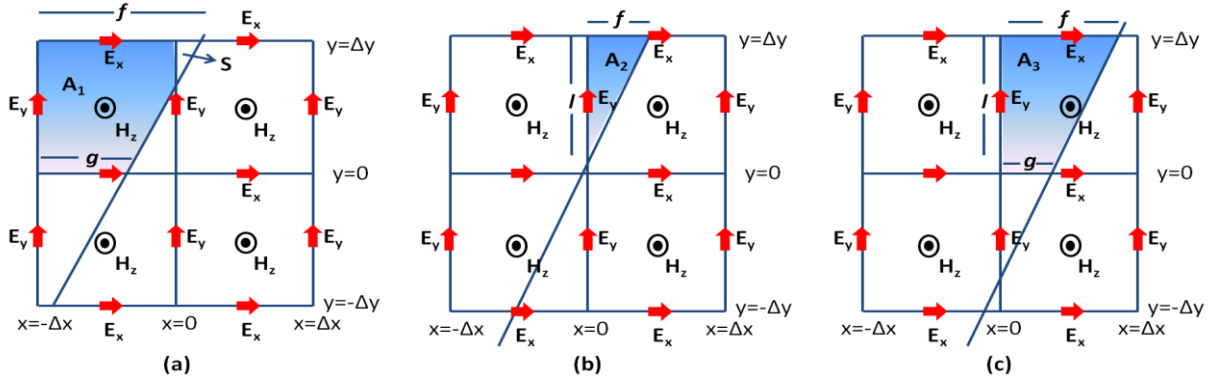


Figure 3.14 Dey-Mittra conformal FDTD scenarios

In all scenarios the PEC is located at the right of the cell cut and TE_z polarization is assumed. In part (a) of figure 3.14, slanted object cross slightly into top right cell. If $s/\Delta x\Delta y$ is less than R_1 which is specific parameter based on numerical stability, we can neglect this penetration and set all four surrounding electric fields to zero for top right cell. On the other hand if we apply Faraday's law and integrate along the contour of area A_1 for top left cell we obtain

$$\begin{aligned}
 H_z^{n+\frac{1}{2}}\left(-\frac{\Delta x}{2}, \frac{\Delta y}{2}\right) &= H_z^{n-\frac{1}{2}}\left(-\frac{\Delta x}{2}, \frac{\Delta y}{2}\right) \\
 &+ \frac{\Delta t}{\mu_0 A_1} \left(E_y^n\left(-\Delta x, \frac{\Delta y}{2}\right) \Delta y + E_x^n\left(-\frac{\Delta x}{2}, \Delta y\right) f - E_x^n\left(-\frac{\Delta x}{2}, 0\right) g \right)
 \end{aligned} \tag{3.131}$$

In part (b) of figure 3.14 the ratio of $A_2/\Delta x\Delta y$ is larger than R_1 . Applying Faraday's Law to the top right cell and integrating over the contour of area A_2 gives the update equation for H_z in the top right cell despite the fact that it is in PEC. Noting that two electric field components resides in pec and set to zero we have:

$$\begin{aligned}
 H_z^{n+\frac{1}{2}}\left(\frac{\Delta x}{2}, \frac{\Delta y}{2}\right) &= H_z^{n-\frac{1}{2}}\left(\frac{\Delta x}{2}, \frac{\Delta y}{2}\right) \\
 &+ \frac{\Delta t}{\mu_0 A_2} \left(E_y^n\left(0, \frac{\Delta y}{2}\right) l + E_x^n\left(\frac{\Delta x}{2}, \Delta y\right) f \right)
 \end{aligned} \tag{3.132}$$

Finally for the part (c) of figure 3.14, applying Faraday's law and integrating along over the contour of area A_3 gives:

$$\begin{aligned}
H_z^{n+\frac{1}{2}}\left(\frac{\Delta x}{2}, \frac{\Delta y}{2}\right) &= H_z^{n-\frac{1}{2}}\left(\frac{\Delta x}{2}, \frac{\Delta y}{2}\right) \\
&+ \frac{\Delta t}{\mu_0 A_3} \left(E_y^n\left(0, \frac{\Delta y}{2}\right) \Delta y + E_x^n\left(\frac{\Delta x}{2} + \Delta y\right) f - E_x^n\left(\frac{\Delta x}{2}, 0\right) g \right)
\end{aligned} \tag{3.133}$$

For all scenarios, electric fields are updated as in conventional Yee's algorithm. The parameter R_1 mentioned previously specifies the smallest area which is included for specification of integration contour. Typically, the choice $R_1 = 0.025$ requires %30 reduction of time step below the normal limit to provide stability. The stability analysis of Day-Mittra conformal technique is analyzed by J.B. Schneider and C.J. Railton [27]. The drawback of reduction of time step will increase total simulation time but it gives very accurate results. The comparison of diffracted field simulation results for stair case approximation and Dey-Mittra conformal FDTD technique is demonstrated in figure 3.15 for a line source illuminated (at 60°) wedge type pec object with 80° vertex angle.

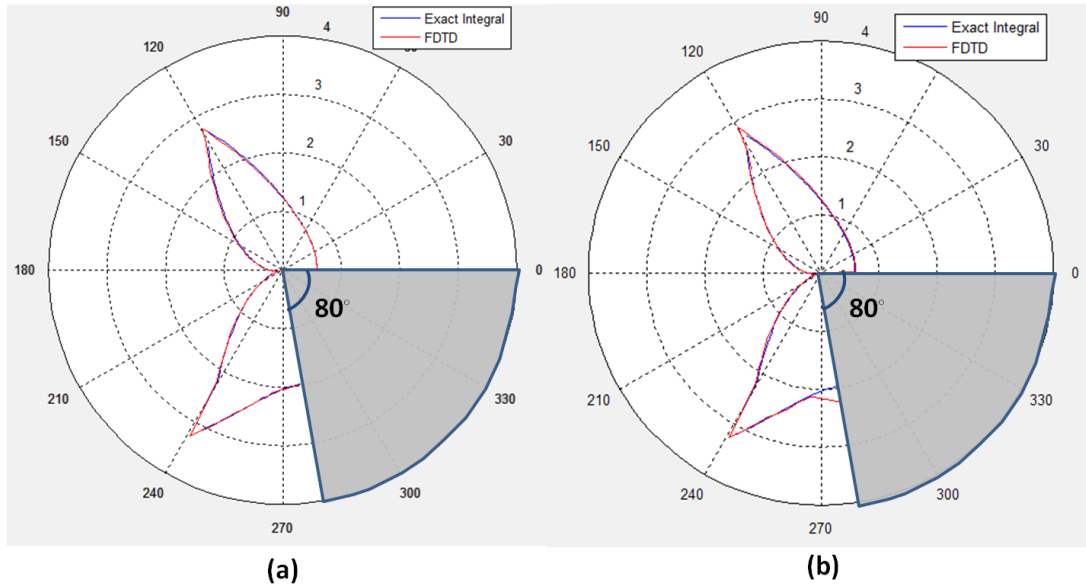


Figure 3.15 Comparison of Dey-Mittra conformal technique (a) and Staircase approximation (b)

It is obvious that, the fields near to the wedge diverge in staircase approximation. Things are getting worse when double-side illumination is of interest. On the other hand, Day-Mittra conformal technique gives very robust result in everywhere. As we see from equations 3.131 through 3.133, the application of conformal FDTD technique requires the calculation of intersection points. This is very tedious process so one can use external meshing software developed for this purpose. In this dissertation, we developed meshing

algorithm and used conformal FDTD algorithm for wedge type PEC object whose codes can be found in the CD given.

3.8 Calculation of Diffracted Fields for Wedge Type Object

The calculation of diffracted fields in FDTD method for PEC wedge object is presented by G.Çakır, L.Sevgi and P.Y.Ufimstev [3]. In this section we will summarize the multi-step processes which is required to extract diffracted fields from total fields. In the first step, we run FDTD simulation with PEC to obtain total fields which includes incident, reflected and diffracted fields as illustrated in figure 3.16 (a).

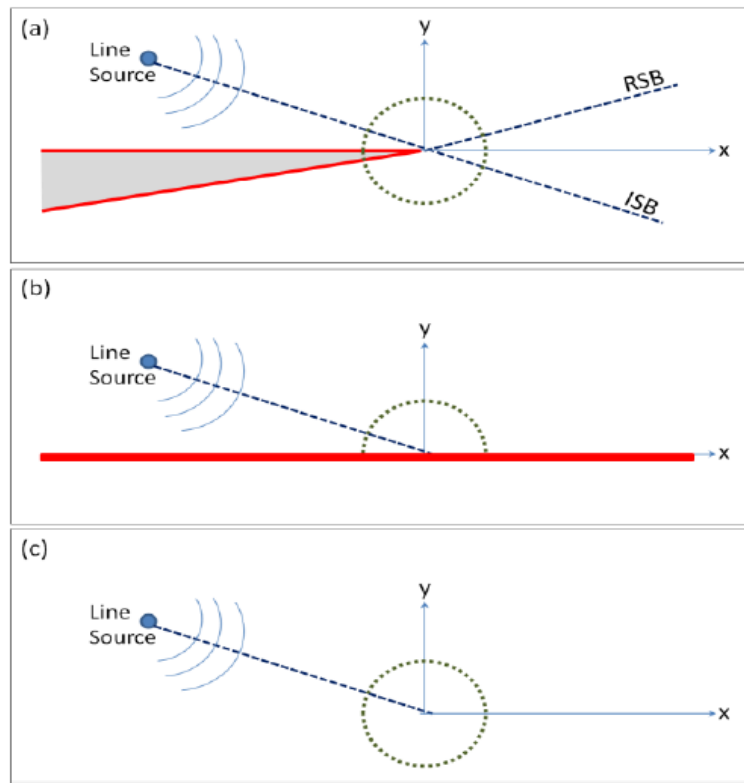


Figure 3.16 Multi-step FDTD-based diffraction approach: (a) The wedge scenario,(b) Infinite-plane problem, (c) Free-space scenario

After obtaining total fields, we stretch the top face of wedge as shown in figure 3.16 (b) and re-run FDTD simulation. Since there is no edge or tip the total fields in this case includes only incident and reflected fields. Finally we remove the wedge in simulation space and re-run FDTD simulation. The total fields obtained from the final step will give only incident fields since there is no object in the simulation space. Subtracting the time data of the second scenario from the first scenario in Region I ($0 \leq \varphi \leq \varphi_0$); and the time

data of the third scenario from the first scenario in Region II ($\pi - \varphi_0 \leq \pi + \varphi_0$) will yield diffracted-only fields all around the wedge. For double side illumination (DSI) that is both faces of the PEC wedge is illuminated with line source, we need four step processes similar to explained previously. In this case we need to repeat step two by stretching bottom face of the wedge.

3.9 WEDGE FDTD GUI and Simulation Examples

The Matlab-based simulation package Wedge FDTD GUI with the front panel displayed in figure 3.17, is prepared for the investigation of wedge diffraction in 2D with FDTD Method and various HFA models. The panel is divided into two parts. The left block is reserved for the structure and FDTD properties. The user also selects either of the TM (Soft) and TE (Hard) boundary conditions and total and diffracted fields, which are calculated multi-step process explained previously, in this block. The right panel is reserved for FDTD visualization and simulation results. User can use the tab located at the top of the right panel to switch between them. The user can also select the colormap which is used for FDTD simulation from the pop-up menu located at the top-right of the panel. Recording property is also enabled for saving FDTD simulation into storage devices in each time step. To do this, one can use record button located at the top-left of the panel. Only avi format is supported and recording feature uses external application embedded in the WEDGE FDTD software so as to reduce file size. What's more, user can see the process of simulation from the progress bar which is shown dynamically during the simulation at the bottom of right panel. The user can expand/shrink the sizes of panels using the divider located between two panels. In this software, we have used Day-Mittra conformal modeling technique to model PEC wedge object. In addition to this, parallel computing feature is used for analytical solutions to achieve faster simulation time. Here we present some simulation examples in figures 3.18 and 3.19. In the first example, we have illuminated to PEC wedge of 30° vertex angle with a TM_z polarized line source from 70 meter distance and 60° angle. We observed total and diffracted fields at 50 meter distance from the PEC with 1.33 degree angle steps. The results are shown at the figure 3.17 and we can say that FDTD simulation results agree with analytical simulation results very well. In the second example we have increased wedge angle to 60° and changed illumination angle to 130° and polarization to TE_z . The simulation results are shown at figure 3.18. In the

first example, we have illuminated to PEC wedge of 30° vertex angle with a TM_z polarized line source from 70 meter distance and 60° angle. We observed total and diffracted fields at 50 meter distance from the PEC with 1.33 degree angle steps. The results are shown at the figure 3.17 and we can say that FDTD simulation results agree with analytical simulation results very well.

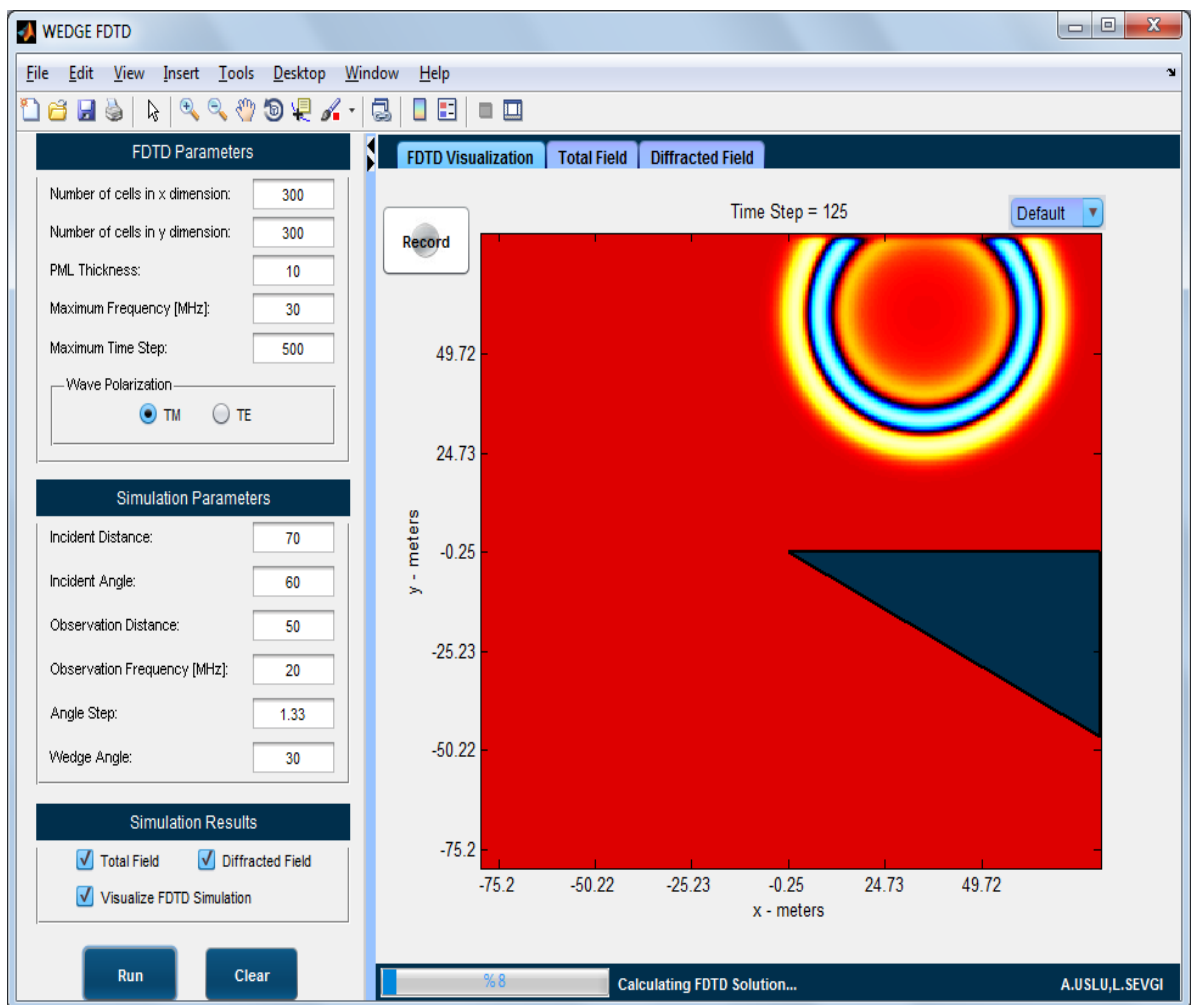


Figure 3.17 Front panel of WEDGE FDTD software

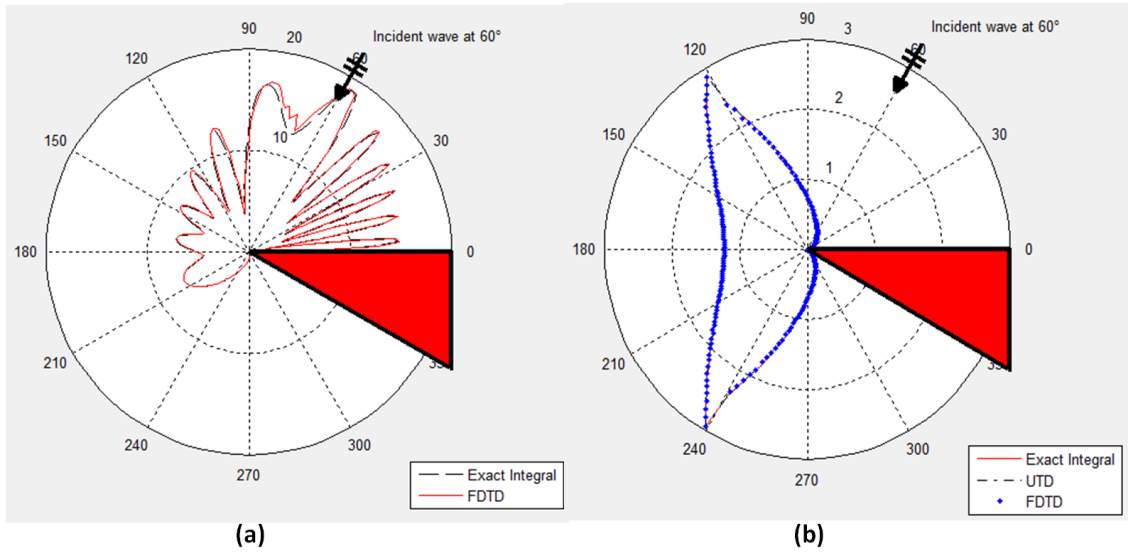


Figure 3.18 Total field, Diffracted field simulation results for TM_z mode

In the second example we have increased wedge angle to 60° and changed illumination angle to 130° and polarization to TE_z . The simulation results are shown at figure 3.19.

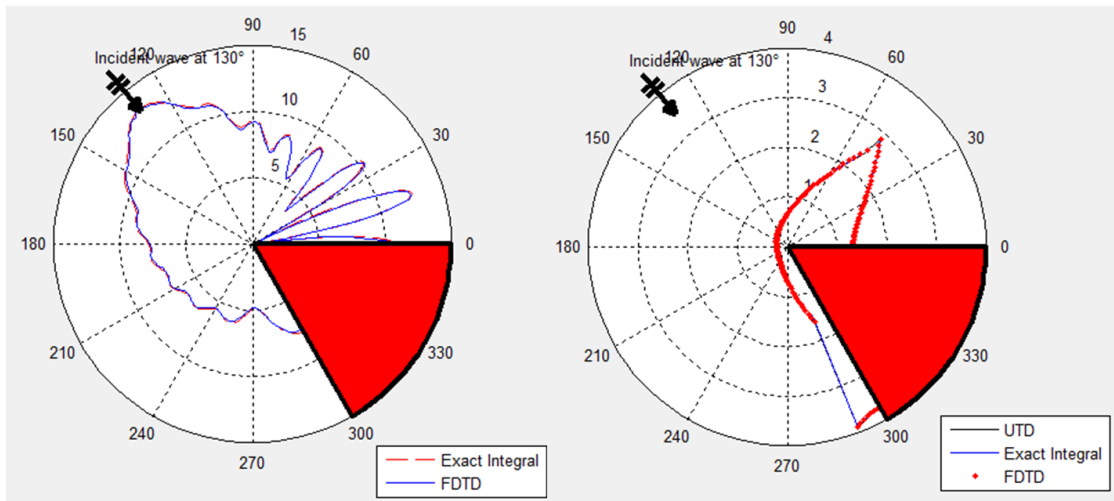


Figure 3.19 Total field, Diffracted field simulation results for TE_z mode

Again we see that, the FDTD simulation results agree with analytical results very well.

3.10 Conclusions

In this chapter, we explained 3D and 2D FDTD technique to obtain numeric results of electromagnetic problems. We have seen that selection of spatial step affects numerical dispersion and selection of time step affects stability. In section 3.6, we reviewed electromagnetic wave propagation at the boundary of two dissimilar media and in

continuation we explain PML theory and algorithm for 3D FDTD lattice. We have seen in section 3.7 that, using staircase approximation for modeling slanted or curved objects can cause non-physical diffracted fields and can lead erroneous results. Also, we have mentioned alternative methods and explained Dey-Mitra conformal FDTD technique as an alternative of staircase method. The multi-step process for extracting diffracted fields from total fields is explained in section 3.8 briefly. Finally in section 3.9, we have introduced a novel Matlab-based virtual tool WEDGE FDTD GUI to analyze 2D wedge scattering problem for both TM_z (Soft) and TE_z (Hard) boundary conditions. We have seen that, FDTD results are almost perfectly fit with the HFA methods.

4 CONCLUSIONS AND FUTURE RESEARCH

4.1 Summary

In this dissertation, we have analyzed non-penetrable wedge scattering problem in 2D space with various HFA techniques and FDTD method. The primary goals of this research were to develop both HFA and FDTD algorithms for obtaining solutions of this type of scattering problem. During this research, we have encountered erroneous diffracted fields which affect the accuracy of the simulation in FDTD side, due to the staircase approximation of Yee algorithm. We have implemented various methods to reduce staircase approximation errors and we have found that Dey-Mittra conformal FDTD technique is optimum and gives best result. For this reason, we have developed CFDTD algorithm for analyzing total and diffracted fields which are formed by the illumination of 2D PEC wedge object, numerically.

We have developed two Matlab-based programs which are WEDGE GUI and WEDGE FDTD GUI for enabling one to investigate scattering behavior of 2D perfect electric conductor (PEC) wedge geometry easily. The former program is dedicated for only analytical solutions. We have used physical optics (PO) method, physical theory of diffraction (PTD) method, unified theory of diffraction (UTD) method, parabolic equation (PE) method with Exact series and Integral methods in this program to analyze wedge scattering phenomena. The latter program uses FDTD method to obtain numeric results of the same problem. In this program, we have used conformal FDTD algorithm for modeling PEC wedge geometry and for analytical comparisons, we have used Exact integral and UTD methods. Being a time domain technique, FDTD method permits us to visualize time domain behavior of the electromagnetic wave. For this reason, we have also implemented this feature with recording option in WEDGE FDTD GUI.

4.2 Future Work

We plan to analyze scattering behavior of PEC or dielectric double wedge geometry in 2D. After that, we may extend our analysis to three dimensional space. Since we have eliminated modeling problems in FDTD, we can easily obtain numerical solutions of three dimensional PEC or dielectric wedge geometries. But deriving 3D analytical solutions seems to be uneasy and we may deal with on this subject.

REFERENCES

1. F. Hacivelioglu, L. Sevgi, P. Ya. Ufimtsev, "Electromagnetic Wave Scattering from a Wedge with Perfectly Reflecting Boundaries: Analysis of Asymptotic Techniques," *IEEE Antennas and Propagation Magazine*, **53**, 3, Jun 2011, pp:232-253.
2. F. Hacivelioglu, L. Sevgi, P. Ya. Ufimtsev, "On the Numerical Evaluations of Diffraction Formulas for the Canonical Wedge Scattering Problem," *IEEE Antennas and Wireless Propagation Letters*, (submitted) 2011.
3. G. Çakır, L. Sevgi, P. Ya. Ufimtsev, "FDTD Modeling of Electromagnetic Wave Scattering from a Wedge with Perfectly Reflecting Boundaries: Comparisons against Analytical Models and Calibration," *IEEE Trans. on Antennas and Propagat.*, Aug 2011.
4. A. Sommerfeld, "Mathematische Theorie der Diffraction," *Mathematische Annalen*, **16**, 1896, pp. 317-374.
5. H. M. Macdonald, *Electric Waves*, The University Press, Cambridge, England, 1902, pp. 186-198.
6. A. Sommerfeld, *Theorie der Beugung*, Chapter 20 in the book "*Die Differential- und Integralgleichungen der Mechanik und der Physik*", The second (Physical) part. Editors: Ph. Frank and R. Mises, Friedr. Vieweg & Sohn, Braunschweig, Germany, 1935. American publication by Mary S. Rosenberg, New York, 1943.
7. C. Hansen, Ed., *Geometrical Theory of Diffraction*, IEEE Press, 1981.
8. J.J. Bowman, T.B.A. Senior, P.L.E. Uslenghi, Eds., *Electromagnetic and Acoustic Scattering by Simple Shapes*, Hemisphere Publishing Corporation, 1987.
9. Yu. A. Kravtsov, N.Y. Zhu, *Theory of Diffraction: Heuristic Approaches*, Alpha Science Series on Wave Phenomena, 2010.
10. P. Ya. Ufimtsev, *Theory of Edge diffraction in Electromagnetics: Origination & Validation of PTD*, SciTech Publishing, Inc., 2009.
11. P. Ya. Ufimtsev, *Fundamentals of the Physical Theory of Diffraction*, Wiley & Sons, Inc., Hoboken, New Jersey, 2007.
12. J. B. Keller, "The geometric optics theory of diffraction," presented at the 1953 McGill Symp. Microwave Optics, A. F. Cambridge Res. Cen. Rep. TR-59-118 (II), 1959, pp:207-210.

13. R. G. Kouyoumjian and P. H. Pathak, "A uniform geometrical theory of diffraction for an edge in a perfectly conducting surface," *Proc. IEEE*, **62**, pp. 1448–1461, Nov. 1974.
14. P. Ya. Ufimtsev, "New Insight into the Classical Macdonald Physical Optics Approximation," *IEEE Antennas & Propagation Magazine*, **50**, 3, June 2008, pp. 11–20. Corrections: *IEEE Antennas & Propagation Magazine*, **50**, 4, August 2008, p. 65.
15. P. Ya. Ufimtsev, "On Polarization Coupling in the PO and PTD Approximations," *IEEE Trans. Antennas Propagat.*, **56**, 12, 2008, pp. 3883–3885.
16. P. Ya. Ufimtsev, *Metod Kraevykh Voln v Fizicheskoi Teorii Difraktsii* [*Method of Edge Waves in the Physical Theory of Diffraction*], Sovetskoe Radio, Moscow, 1962. Translated into English by the U.S. Air Force, Foreign Technology Division (National Air Intelligence Center), Wright-Patterson AFB, OH, 1971. Technical Report AD 733203, Defense Technical Information Center of USA, Cameron Station, Alexandria, VA, 22304-6145, USA.
17. P. Ya. Ufimtsev, "Difraktsiya na Kline i Lente" [*Diffraction from Wedge and Strip*], *Zurnal Technicheskoi Fiziki*, **27**, 8, 1957, pp. 1840–1849 [English translation published by *Soviet Physics-Technical Physics*].
18. P. Ya. Ufimtsev, "Transverse Diffusion for Diffraction by a Wedge," *Radio Engineering and Electronic Physics*, **10**, 6, 1965, pp. 866–875.
19. V. A. Fock, *Electromagnetic Diffraction and Propagation Problems*, Pergamon Press, London, 1965.
20. G. D. Malyuzhinets, "Development of Ideas about Diffraction Phenomena," *Soviet Physics-Uspokhi*, **69**, 2, 1959, p. 5.
21. K. S. Yee, "Numerical Solution of Initial Boundary Value Problems Involving Maxwell's Equations in Isotropic Media", *IEEE Trans. Antennas and Propagation*, **14**, 1966, pp. 302–307.
22. U. S. Inan, R. A. Marshall, *Numerical Electromagnetics The FDTD Method*, Cambridge University Press, New York, 2011.
23. A. Taflove, S. C. Hagness, *Computational Electrodynamics: The Finite-Difference Time-Domain Method*, Artech House, INC, Norwood, 2011.
24. J. P. Berenger, *Perfectly Matched Layer (PML) for Computational Electrodynamics*, Morgan & Claypool Publishers, 2007.

25. F. T. Ulaby, *Fundamentals of Applied Electromagnetics*, Prentice Hall, New Jersey, 1997.
26. W. YU, R. Mittra, T.Su, Y.Liu, X. Yang, *Parallel Finite-Difference Time-Domain Method*, Artech House, Norwood, 2006.
27. C. J. Railton, J. B. Scheider, "An Analytical and Numerical Analysis of Several Locally Conformal FDTD Schemes," *IEEE Trans on MTT*, 47 (1), Jan 1999, pp. 56-66.

APPENDIX I

```
%% -----
% TMz Mode 2D Propagation in Free Space
% Author: Alper Uslu
% Method: FDTD
% Date: July 2011
% -----

clear;
clc;
delx=0.002; % Sample size along x direction
dely=delx; % Sample size along y direction
c=299792458; % Speed of Light
f0=278e6; % Frequency
lambda=c/f0; % Wavelength
k=2*pi/lambda; % Wavenumber
delt=delx/(c*2); % Magic Time Step delt*c=delx
epsilon=8.85*10^-12; % Free Space Permittivity
mu=4*pi*10^-7; % Free Space Permeability
nu=sqrt(mu/epsilon); % Free Space Impedance

%% PML Properties

d=10; %PML thickness
rdesired=exp(-16); % Desired reflection coefficient
m=4; % Grading coefficient
sigmaxmax=-(m+1)*log(rdesired)/(2*nu*d*delx); % Maximum electrical
conductivity x direction
sigmaymax=sigmaxmax; % Maximum electrical
conductivity y direction
kzmax=1; % PML parameter
kxmax=1; % PML parameter
kymax=1; % PML parameter

%% Simulation Space Properties
nx=100; % Free space region total number of samples
ny=100; % Free space region total number of samples

nxx=nx+1; % Free space region total number of
samples+1
nyy=ny+1; % Free space region total number of
samples+1
dd=d+1; % PML Thickness + 1
nxtot=nx+2*d; % Total Simulation Space number of samples
nytot=ny+2*d; % Total Simulation Space number of samples
nxxtot=nxtot+1; % Total Simulation Space number of samples
+ 1
nyytot=nytot+1; % Total Simulation Space number of samples
+ 1

%% Coefficient Matrices

Ez=zeros(nxxtot,nyytot); % Ez field array
Dz=zeros(nxxtot,nyytot); % Dz field array

Hx=zeros(nxxtot,nyytot); % Hx field array
```

```

Bx=zeros (nxxtot,nytot);           % Bx field array

Hy=zeros (nxtot,nyytot);           % Hy field array
By=zeros (nxtot,nyytot);           % By field array

C1ez=zeros (size (Ez) );           % 1.coefficient array used calculation of Dz
C2ez=zeros (size (Ez) );           % 2.coefficient array used calculation of Dz
C3ez=zeros (size (Ez) );           % 1.coefficient array used calculation of Ez
C4ez=zeros (size (Ez) );           % 2.coefficient array used calculation of Ez
C5ez=zeros (size (Ez) );           % 3.coefficient array used calculation of Ez
C6ez=zeros (size (Ez) );           % 4.coefficient array used calculation of Ez

D1hx=zeros (size (Hx) );           % 1.coefficient array used calculation of Bx
D2hx=zeros (size (Hx) );           % 2.coefficient array used calculation of Bx
D3hx=zeros (size (Hx) );           % 1.coefficient array used calculation of Hx
D4hx=zeros (size (Hx) );           % 2.coefficient array used calculation of Hx
D5hx=zeros (size (Hx) );           % 3.coefficient array used calculation of Hx
D6hx=zeros (size (Hx) );           % 4.coefficient array used calculation of Hx

D1hy=zeros (size (Hy) );           % 1.coefficient array used calculation of By
D2hy=zeros (size (Hy) );           % 2.coefficient array used calculation of By
D3hy=zeros (size (Hy) );           % 1.coefficient array used calculation of Hy
D4hy=zeros (size (Hy) );           % 2.coefficient array used calculation of Hy
D5hy=zeros (size (Hy) );           % 3.coefficient array used calculation of Hy
D6hy=zeros (size (Hy) );           % 4.coefficient array used calculation of Hy

%----- Coefficients for outside PML region-----
C1=1;
C2=delt;
C3=1;
C4=1/(2*epsilon*epsilon);
C5=2*epsilon;
C6=2*epsilon;

D1=1;
D2=delt;
D3=1;
D4=1/(2*epsilon*mu);
D5=2*epsilon;
D6=2*epsilon;

C1ez (d+1:nxxtot-d, :)=C1;
C2ez (d+1:nxxtot-d, :)=C2;
C3ez (:,d+1:nyytot-d)=C3;
C4ez (:,d+1:nyytot-d)=C4;
C5ez (:, :)=C5;
C6ez (:, :)=C6;

D1hx (:,d+1:nytot-d)=D1;
D2hx (:,d+1:nytot-d)=D2;
D3hx (:, :)=D3;
D4hx (:, :)=D4;
D5hx (d+1:nxxtot-d, :)=D5;
D6hx (d+1:nxxtot-d, :)=D6;

D1hy (:, :)=D1;
D2hy (:, :)=D2;

```

```

D3hy(d+1:nxtot-d,:) = D3;
D4hy(d+1:nxtot-d,:) = D4;
D5hy(:,d+1:nyytot-d) = D5;
D6hy(:,d+1:nyytot-d) = D6;

%-----
%-----Coefficients for PML Region-----

for i=1:d
    q=d-i-0.5; % Since Hy component's i index located at 1/2 steps
    sigmax=(q/d)^m*sigmaxmax; % Polynomial Grading
    kx=1+(kxmax-1)*(q/d)^m; % Polynomial Grading

    D3hy(i,:)=(2*epsilon*kx-sigmax*delt)/(2*epsilon*kx+sigmax*delt);
    D3hy(nxtot-i+1,:)=(2*epsilon*kx-
sigmax*delt)/(2*epsilon*kx+sigmax*delt);

    D4hy(i,:)=1/((2*epsilon*kx+sigmax*delt)*mu);
    D4hy(nxtot-i+1,:)=1/((2*epsilon*kx+sigmax*delt)*mu);

    sigmax=((d-i)/d)^m*sigmaxmax; % Polynomial Grading
    kx=1+(kxmax-1)*((d-i)/d)^m; % Polynomial Grading

    Clez(i,:)=(2*epsilon*kx-sigmax*delt)/(2*epsilon*kx+sigmax*delt);
    Clez(nxxtot+1-i,:)=(2*epsilon*kx-
sigmax*delt)/(2*epsilon*kx+sigmax*delt);

    C2ez(i,:)=(2*epsilon*delt)/(2*epsilon*kx+sigmax*delt);
    C2ez(nxxtot+1-i,:)=(2*epsilon*delt)/(2*epsilon*kx+sigmax*delt);

    D5hx(i,:)=2*epsilon*kx+sigmax*delt;
    D5hx(nxxtot-i+1,:)=2*epsilon*kx+sigmax*delt;

    D6hx(i,:)=2*epsilon*kx-sigmax*delt;
    D6hx(nxxtot-i+1,:)=2*epsilon*kx-sigmax*delt;

end

%PEC walls outside the PML
C1ez(1,:) = -1.0;
C1ez(nxxtot,:) = -1.0;
C2ez(1,:) = 0.0;
C2ez(nxxtot,:) = 0.0;

for j=1:d
    q=d-j-0.5; % Since Hx component's j index located at 1/2 steps
    sigmay=(q/d)^m*sigmaymax; % Polynomial grading
    ky=1+(kymax-1)*(q/d)^m; % Polynomial grading

    D1hx(:,j)=(2*ky*epsilon-sigmay*delt)/(2*ky*epsilon+sigmay*delt);
    D1hx(:,nytot-j+1)=(2*ky*epsilon-
sigmay*delt)/(2*ky*epsilon+sigmay*delt);
    D2hx(:,j)=2*epsilon*delt/(2*ky*epsilon+sigmay*delt);
    D2hx(:,nytot-j+1)=2*epsilon*delt/(2*ky*epsilon+sigmay*delt);

```

```

sigmay=((d-j)/d)^m*sigmaymax; % Polynomial grading
ky=1+(kymax-1)*((d-j)/d)^m; % Polynomial grading

C3ez(:,j)=(2*ky*epsilon-sigmay*delt)/(2*ky*epsilon+sigmay*delt);
C3ez(:,nyytot-j+1)=(2*ky*epsilon-
sigmay*delt)/(2*ky*epsilon+sigmay*delt);
C4ez(:,j)=1/((2*epsilon*ky+sigmay*delt)*epsilon);
C4ez(:,nyytot-j+1)=1/((2*epsilon*ky+sigmay*delt)*epsilon);

D5hy(:,j)=2*epsilon*ky+sigmay*delt;
D5hy(:,nyytot-j+1)=2*epsilon*ky+sigmay*delt;
D6hy(:,j)=2*epsilon*ky-sigmay*delt;
D6hy(:,nyytot-j+1)=2*epsilon*ky-sigmay*delt;
end

% PEC Walls
C3ez(:,1)=-1;
C3ez(:,nyytot)=-1;
C4ez(:,1)=0;
C4ez(:,nyytot)=0;
%-----

%% Source and Simulation Time Properties
rtau=50.0e-12;
tau=rtau/delt;
ndelay=3*tau;
J0=-1.0*epsilon;
T=350; % Total number of time steps
%% FDTD Calculation
for t=0:T

    Bstore=Bx;

    Bx(2:nxtot,:)=D1hx(2:nxtot,:).* Bx(2:nxtot,:)-...
        D2hx(2:nxtot,:).*(Ez(2:nxtot,2:nyytot)-
Ez(2:nxtot,1:nyytot))./dely;

    Hx(2:nxtot,:)= D3hx(2:nxtot,:).*Hx(2:nxtot,:)+...
        D4hx(2:nxtot,:).*(D5hx(2:nxtot,:).*Bx(2:nxtot,:)-
...

D6hx(2:nxtot,:).*Bstore(2:nxtot,:));
    Bstore=By;
    By(:,2:nyytot)=D1hy(:,2:nyytot).* By(:,2:nyytot)-...
        D2hy(:,2:nyytot).*(-...
(Ez(2:nxtot,2:nyytot)-
Ez(1:nxtot,2:nyytot)))./delx;

    Hy(:,2:nyytot)= D3hy(:,2:nyytot).*Hy(:,2:nyytot)+...
        D4hy(:,2:nyytot).*(D5hy(:,2:nyytot).*By(:,2:nyytot)-
...

D6hy(:,2:nyytot).*Bstore(:,2:nyytot));

```



```

    Dstore=Dz;
    Dz(2:nxtot,2:nytot)=C1ez(2:nxtot,2:nytot).* Dz(2:nxtot,2:nytot)+...
        C2ez(2:nxtot,2:nytot).*(Hy(2:nxtot,2:nytot)-...
Hy(1:nxtot-1,2:nytot))-...

    (Hx(2:nxtot,2:nytot)-Hx(2:nxtot,1:nytot-1))./delx;

    Dz(60,60)=Dz(60,60)+J0*(t-ndelay)*exp(-(t-ndelay)^2/tau^2));

    Ez(2:nxtot,2:nytot)=C3ez(2:nxtot,2:nytot).*Ez(2:nxtot,2:nytot)+...
    C4ez(2:nxtot,2:nytot).*(C5ez(2:nxtot,2:nytot).*Dz(2:nxtot,2:nytot)-...
    C6ez(2:nxtot,2:nytot).*Dstore(2:nxtot,2:nytot));

    %% Plot Ez at every time step
    surf(Ez);
    shading interp; lighting phong; colormap hot; axis off; zlim([0 1]);
    set(gcf,'Color',[0 0 0],'Number','off','Name',sprintf('Time
Step = %i', t));

    pause(0.05);
end

```

BIOGRAPHY

Alper USLU was born in Bolu/Turkey and received his B.Sc. in electronics and communications engineering, Dogus University, Turkey, in 2010. Between 2005-2010 he has worked as a Senior software developer and embedded system designer. He was granted to Leopold. B. Felsen Excellence in Electrodynamics award on 1 August 2011. Currently, he has two journal/magazine papers and two conference papers.